A quantitative rule to explain multi-spine plasticity

T. E. Chater[1,*], M.F. Eggl[2,*], Y. Goda[1,3,#,†], and T. Tchumatchenko [2,4,#,‡]

[1]Laboratory for Synaptic Plasticity and Connectivity, RIKEN Center for Brain Science, Wako-shi, Saitama, Japan
[2]University of Mainz Medical Center, Anselm-Franz-von-Bentzel-Weg 3, 55128 Mainz, Germany
[3]Synapse Biology Unit, Okinawa Institute for Science and Technology Graduate University, Onna-son, Kunigami-gun, Okinawa, Japan
[4] Institute of Experimental Epileptology and Cognition Research, University of Bonn Medical Center, Venusberg-Campus 1, 53127 Bonn, Germany
[*]These authors contributed equally
[#]These authors contributed equally, corresponding authors

Abstract

Neurons receive thousands of inputs onto their dendritic arbour, where individual synapses undergo activity-dependent changes in strength. The durable forms of synaptic strength change, long-term potentiation (LTP) and long-term depression (LTD), require calcium entry through N-methyl-D-aspartate receptors (NMDARs) that triggers downstream protein signalling cascades in the dendrite. Intriguingly, sLTP and sLTD are not necessarily restricted to the active, targeted synapses (homosynapses), and the changes in synaptic strength can spread and affect the strengths of inactive or non-stimulated synapses (heterosynapses) on the same cell. Precisely how neurons allocate resources for implementing the changes in strength at individual synapses depending on their proximity to activity across space and time remains an open question. In order to gain insights into the elementary processes underlying heterosynaptic plasticity and their interplay with homosynaptic plasticity, we have combined experimental and mathematical modelling approaches. On the one hand, we used glutamate uncaging to precisely and systematically stimulate variable numbers of homosynapses sharing the same dendritic branch whilst monitoring tens of other heterosynapses on the same dendrite. Homosynaptic potentiation of clusters of dendritic spines leads to heterosynaptic changes that are NMDAR-dependent, requiring CaMKII and calcineurin activity. On the other hand, inspired by the calcium levels hypothesis where different amounts of calcium lead to either growth or shrinkage of spines, we have built a model based on a dual-role calcium-dependent protein that induces spine shrinkage or potentiation dynamics. Comparing our experimental results with model predictions, we find that *(i)* both collaboration and competition among spines for protein resources are key drivers of heterosynaptic plasticity and *(ii)* the temporal and spatial distance between simultaneously stimulated spines impact the resulting spine dynamics. Moreover, our model can reconcile a number of disparate and sometimes contradictory experimental reports of heterosynaptic sLTP or sLTD at homo and heterosynaptic spines. Our results provide a quantitative description of the heterosynaptic footprint unfolding across minutes and hours post-stimulation across tens of microns of dendritic space. This broadens our knowledge about the operation of non-linear dendritic summation rules and how they impact spiking decisions.

Introduction

A typical neuron in the mammalian brain hosts thousands of synapses along its dendritic arbour. Spikes arriving at the synapses can drive changes in the size and molecular composition of the corresponding postsynaptic dendritic spines and induce synaptic potentiation or depression. In classical Hebbian synaptic plasticity, the change is long-lasting and thought to be specific to active synapses (i.e. homosynapses) and independent of other synapses. Interestingly, synapses that are not directly stimulated (i.e. heterosynapses) on the same postsynaptic target neuron can be modulated nonetheless to undergo synaptic strength changes by homosynaptic

[†]yukiko.goda@oist.jp
[‡]tatjana.tchumatchenko@uni-mainz.de

activity (reviewed in Chater and Goda (2021)). The polarity of heterosynaptic plasticity can either follow the homosynaptic changes, oppose them, or both, (Oh et al., 2015; Engert and Bonhoeffer, 1997; Fitzsimonds et al., 1997; Royer and Paré, 2003).

Specifically, heterosynaptic changes can occur locally on the same dendrite (Oh et al., 2015), spread to distant dendritic compartments (for example, apical to basal, straddling the cell body, Lynch et al. (1977)), or be transmitted to the presynaptic compartment (Tong et al., 2021) and up- or down-regulate the strengths of multiple synapses at a time.

Importantly, the influence of homosynaptic stimulation is not limited to unstimulated nearby spines, but they themselves are affected by the cross-talk of stimulated and unstimulated spines (Makino and Malinow, 2011; Lee et al., 2016). When more than two plasticity induction events interfere in space and time, predicting their respective magnitude remains a challenge. This plasticity interference has a critical influence on spike generation downstream and has been linked to important circuit functions (Caroni et al., 2012; Fu et al., 2012; Hensch, 2005), but many questions about the rules governing the plasticity summation rules and their molecular underpinning are still open.

Different functional roles for heterosynaptic plasticity have been proposed according to how heterosynapses are affected. For example, heterosynaptic changes of the opposite polarity to homosynaptic changes may act to balance the total synaptic input activity received by a neuron within some predefined range and thus serve a compensatory, homeostatic function (for example Lynch et al. (1977); Royer and Paré (2003)). On the other hand, heterosynaptic changes of the same polarity as the homosynaptic plasticity (for example, the spreading of potentiation) have been proposed as a way for neurons to cluster inputs onto their dendritic arbours according to the activity patterns. Indeed, clusters of coactive inputs have been observed in many brain regions (dentate gyrus to CA3, Chicurel and Harris (1992); CA3 to CA1, Druckmann et al. (2014); somatosensory cortex, Kasthuri et al. (2015)), and at least in CA1 pyramidal neurons, spontaneous synchronous calcium transients mediate their assembly (Lee et al., 2016).

Despite the large body of work on heterosynaptic plasticity, the elementary processes that instruct heterosynaptic inputs and the effective spatio-temporal footprint that evolves across minutes along the dendritic arbour are still not fully understood (Chater and Goda, 2021). In part, this is a combinatorial problem that needs to be studied with defined spatial and temporal distances between stimulated and unstimulated synapses across several minutes and requires a model framework to explain the observed effects.

In broad terms, homosynaptic activity leads to a flux of calcium ions into the postsynaptic neuron through NMDARs and voltage-gated calcium channels (VGCCs), which then engages a wide range of calcium-dependent signalling events that spread from homosynapses along the dendrite to neighbouring spines, including the spread of calcium itself. A mechanism involving membrane voltage signals can also contribute to heterosynaptic plasticity. Dendrites display non-linearities in their signal integration and can boost the amplitude of synaptic responses if they are activated closely in space and/or time (e.g. Major et al. (2008); Branco and Häusser (2011). For example, the generation of NMDA spikes, in turn, elicits substantial local depolarisation in the dendrite, which then backpropagates into neighbouring spines (Schiller et al., 2000). Such spikes may allow segments of dendrites to function as independent computational units within the neuron (Polsky et al., 2004) while promoting communication to nearby heterosynaptic inputs and influencing their propensity to undergo plasticity. The contribution of secondary events such as local translation, in which synaptic activity leads to bouts of *de novo* protein synthesis in the dendrite, adds an additional layer of regulation. The newly synthesised proteins are available for sequestration by nearby synapses that may involve competition between spines. The precise manner in which neurons achieve heterosynaptic distribution of new proteins is still under debate, with proposed mechanistic frameworks that include the synaptic tag and capture (STC) (Redondo and Morris, 2011) and the clustered plasticity model where the influence of plasticity is confined to individual dendritic branches (Govindarajan et al., 2006).

Many candidate molecules have been identified as potential mediators of heterosynaptic signalling. These include the calcium-calmodulin dependent protein phosphatase calcineurin (Oh et al., 2015; Tong et al., 2021), the calcium-calmodulin dependent protein kinase CaMKII (Rose et al. (2009) but see Lee et al. (2009)), the small GTPases Ras (Harvey and Svoboda, 2007) and RhoA (Murakoshi et al., 2011), and the diffusible gas nitric oxide (Tong et al., 2021) amongst others (reviewed in Yasuda and Murakoshi (2011)). Following homosynaptic activity, several of these molecules have been shown to diffuse away from the activated spine and traverse locally along the dendrite segment; heterosynaptic strengths are affected with a time course on the order of tens of milliseconds to tens of seconds (Letellier et al., 2019). Other components of the plasticity response are confined

to the activated spine (for example, Cdc42 and potentially CaMKII, see Murakoshi et al. (2011) and Lee et al. (2009)). CaMKII and calcineurin work in parallel to sense synaptic activity and readout frequency and strength of the stimulus (Fujii et al., 2013), and in particular, calcineurin has been implicated in heterosynaptic depression (Oh et al., 2015). Mouse lacking calcineurin have a deficit in sLTD (Mulkey and Malenka, 1992), whilst loss or inhibition of CaMKII isoforms leads to deficits in sLTP and memory (e.g., Silva et al. (1992); Tan and Liang (1996)). Hence, activation of synaptic protein kinases and phosphatases following calcium entry might be a critical determinant of the allocation or activation of essential plasticity components at neighbouring spines for the expression of heterosynaptic plasticity.

Overall, the current knowledge of molecular cascades highlights the existence of cooperative mechanisms that can jointly upregulate multiple homosynaptic and heterosynaptic sites (e.g. *de novo* protein synthesis) and the contribution of counter-forces that can dampen the synaptic response (e.g. protein resource sharing). Towards the goal of clarifying the underlying basis of heterosynaptic coordination that neurons use to integrate information received by their dendrites, we asked whether we can quantitatively predict the spatio-temporal footprint of heterosynaptic plasticity resulting from the activity of a particular set of homosynapses based on the knowledge of molecular players of plasticity. To this end, we combined experimental and modelling approaches and explored the minimal principle components that drive heterosynaptic spine plasticity. Using glutamate uncaging, we systematically elicited structural sLTP (sLTP: Matsuzaki et al. (2004) Harvey and Svoboda (2007)) at variable numbers of target single spines and monitored the homosynaptic and heterosynaptic spine structural dynamics over time while also testing their sensitivity to perturbing candidate heterosynaptic signalling systems. In parallel, we then built a mathematical model in which the action of calcium and protein dynamics within the dendrite results in sLTP or sLTD at homosynaptic and heterosynaptic sites depending on the context in which activity is imposed.

Our experimental results show that the plasticity response was strongly affected by the number and the spatial arrangement of quasi-simultaneously stimulated spines. Hereby a weaker average spine response was associated with glutamate uncaging at more synaptic sites, and the size of the average spine growth was inversely proportional to the distance to its nearest stimulated neighbours. Furthermore, the spines that were located within a cluster of stimulated spines but were not themselves stimulated showed responses similar to their stimulated neighbours, albeit at a reduced amplitude. Crucially, the mathematical model could accurately predict homosynaptic and heterosynaptic spine dynamics as measured in our experiments. Collectively, our results provide novel insights into competitive and collaborative mechanisms that allocate plasticity factors across spines as a function of temporal and spatial distance from the sites of induction of plasticity and, in turn, determine the plasticity response at individual spines.

Results

On the experimental side, we began our study by eliciting sLTP and assessing the structural plasticity at neighbouring heterosynaptic spines sharing a dendrite. To this end, we used glutamate uncaging to quasi-synchronously stimulate a handful of spines belonging to target homosynapses (n = 1, 3, 7, 15) in CA1 pyramidal neurons in rat organotypic hippocampal slices. Prior biolistic transfection of the neuron with GFP allowed visualisation of the entire dendritic tree and individual spines of both homosynapses and heterosynapses. As reported previously, robust sLTP was observed at target stimulated spines (Figure 1, Figure S1).

To investigate the minimal molecular requirements for triggering sLTP or sLTD at heterosynapses in association with sLTP induction at homosynapses, we built a mathematical model based on molecular actors that have been consistently implicated in the regulation of long-term synaptic plasticity. Our model considers fast dynamics of calcium-binding proteins (CBP) that trigger a protein redistribution that evolves on the time scale of minutes to hours. Specifically, we consider experimentally reported features of Ca^{2+}-dependent activation of CaMKII and the regulatory influence of calcineurin on spine plasticity.
Inducing sLTP triggers a fast Ca^{2+} rise that in turn activates CBP at the site of stimulation and its surroundings. The initial peak in CBP concentration at the sLTP site is set at C_0 and decays over time with a rate α;

$$\frac{\partial C}{\partial t} = -\alpha C. \tag{1}$$

Spatially, C_0 is highest at the sLTP site and declines with distance from the sLTP site along the dendrite length. At individual spines, the local CBP concentration has a spine-specific component that cannot be shared across spines and a common fraction at the dendritic base. The common fraction is reduced proportionally to the number of simultaneously stimulated spines in the spatial vicinity of an sLTP spine as follows

$$C(0) = C_d(0)/N + C_s(0). \tag{2}$$

As sLTP is induced at more spines, we hypothesize that more spines will compete for a potentiation factor that critically relies on the dendritic component of CBP, C_d, thus decreasing the amount available for each sLTP spine. However, this amount will be lower the more spines compete. Therefore, we hypothesize that inducing sLTP at more spines (glutamate uncaging at more spines) leads to the average potentiation of each sLTP spine decreasing proportionally to the number of spines until a baseline is reached, which corresponds to the baseline $C_s(0)$. Similarly, all spines, including the heterosynaptic spines that do not receive direct stimulation, have C_s at their disposal such that a baseline amount of CBP-driven potentiation is possible regardless of the number of sLTP events.

We further introduce a protein resource P that is recruited by the local CBP concentration and leaves the spine of interest at a rate β_2

$$\frac{\partial P}{\partial t} = \beta_1 C - \beta_2 P. \tag{3}$$

The variable P describes the concentration of activated protein that mediates the long-term spine potentiation that lasts tens of minutes or more. P is inspired by the experimental observation that CaMKII, which is involved in sLTP, is activated by an increase in Ca^{2+} (Urakubo et al., 2014). Moreover, the active state of CaMKII can be converted into a Ca^{2+}-independent, persistently active state via the process of autophosphorylation (Glazewski et al., 2000). We return to the involvement of CaMKII in sLTP below. The concentration of P grows as long as the accumulation rate is larger than the rate at which the protein leaves the spine. Whether a spine grows in size or shrinks over the long term depends on the concentrations of CBP and P, in line with experimental reports (Jaffe et al., 1992). If P is above the potentiating threshold, it will contribute a potentiating force. On the other hand, if P is below the depression threshold, it will trigger spine shrinkage. For the model, we postulate that similarly to the dendritic CBP term C_d, P also contains two components: a dendritic component P_d that is shared across spines and a spine-specific reservoir P_s. Accordingly, the initially available $P(0)$ is reduced as N sLTP sites are added,

$$P(0) = P_d(0)/N + P_s(0). \tag{4}$$

Fig. 1 presents a schematic of the model along with a graphic summary of its action. The spine and dendritic distribution of Ca^{2+}-binding protein (CBP) in basal conditions (Fig. 1c) undergoes a change upon the simultaneous induction of sLTP (here at two spines for illustration purposes: Fig. 1d); CBP concentration increases in each stimulated spine along with activation of P (increase in P, red circles in Fig. 1d). In Fig. 1e, we summarize the model equations describing the CBP and P dynamics and the resulting spine changes. P can be associated with either potentiation or depression of spines (Fig. 1f), whereby the threshold for potentiation or depression is ν_1 or ν_2, respectively.

The relative outcomes of spine sLTP or sLTD as function of C, P, ν_1 and ν_2, or the difference between ν_1 and ν_2 are shown (Fig. 1g-i). If a spine has a low CBP value (low C) due to a lack of sLTP at this site and without a sufficient CBP spillover from other (nearby) activated spines, the concentration of P also cannot grow as a result, and the spine will depress (blue regime). This model suggests that one way to ensure robust potentiation of heterosynaptic spines is to trigger simultaneous sLTP events at multiple closely located spines such that CBP concentrations from individual sLTP events overlap at the heterosynaptic spines, raising P and reaching the potentiation domain (red area: Fig. 1g). Varying the depression threshold and the relative distance between the potentiation and depression thresholds, we find robust potentiation if the difference between the two thresholds is small (Fig. 1h). In summary, the model makes three main experimentally testable predictions. First, raising the ratio of the potentiation threshold ν_1 over the initially available P_0 is expected to reduce potentiation at the stimulated spines on the short and long time scales. On the other hand, lowering the ratio of ν_1 over the P_0 will increase potentiation at stimulated spines at short time scales but will leave long time scales largely unaffected because the long-term potentiation value is a non-linear function of the threshold difference

$\nu_1 - \nu_2$. Second, our model predicts that simultaneous sLTP events at multiple closely located spines will trigger potentiation of neighbouring heterosynaptic spines due to an overlap in CBP, provided that a sufficient amount of P is available. Moreover, the potentiation at heterosynaptic spines grows proportionally with the number of simultaneous sLTP induction events in their immediate vicinity, particularly the long-term component of heterosynaptic potentiation. However, past a certain point when P becomes limiting, the potentiation at heterosynaptic spines will decrease proportionally to the number of sLTP events. Third, the dynamics predict that increasing the spatial distance between simultaneous sLTP events will decrease the potentiation strength until a certain distance is reached, which uncouples the sLTP events as single independent events.

Role of potentiation and depression thresholds for the spine response

In order to determine the robustness of the model, we experimentally tested the three major predicted outcomes in the sLTP paradigm using glutamate uncaging described above. The first prediction of our model posits that raising the potentiation threshold ν_1 will reduce the extent of potentiation observed at the stimulated spines on both short and long time scales, whereas lowering the potentiation threshold will increase the extent of potentiation at stimulated spines on short time scales alone. As described above, the variable P was motivated by Ca^{2+}-dependent properties of CaMKII and its involvement in long-term potentiation. To increase the sLTP threshold, therefore, we inhibited CaMKII with myristoylated autocamtide-inhibitory peptide (AIP), a specific competitive inhibitor of CaMKII (Ishida et al., 1995). In contrast, the sLTP threshold was decreased by taking advantage of calcineurin that promoted sLTD, and we triggered sLTP in the presence of calcineurin blocker FK506 (Dumont, 2000).

Fig. 2a) illustrates the dendritic segment containing the stimulated spine (blue ROI and a blue arrow; see methods section for the algorithm for the ROI assignment) 15 min before sLTP induction from a representative experiment. The fluorescence intensity of the stimulated spine or sham unstimulated spine was analysed before and after sLTP induction over a 55 min recording period. The mean spine fluorescence intensity change normalised to the pre-stimulation baseline (Fig. 2b)) can be accurately fitted by our model to the experimentally observed sLTP, despite the presence at $t = 30$ min of a single outlier spine (see S3a). The sham non-stimulated spines remained stable over the recording period, indicating a lack of adverse effects of uncaging laser pulses.

We then repeated the experiment in the presence of AIP (5μM) or FK506 (2μM). Consistent with previous reports (e.g. Oh et al. (2015); Tong et al. (2021)), a robust increase in early spine potentiation was observed in the presence of FK506 relative to control. In contrast, potentiation was reduced over both short and long time scales in the presence of AIP compared to control (Fig. 2d-f). The model fits (solid lines, Fig. 2d) indicate that, in the presence of FK506, there is a significant drop in both ratios of the thresholds ν_1 and ν_2 with respect to P_0. In the presence of AIP, ν_2 increased to favour synaptic depression, which resulted in a significantly weaker sLTP response at the stimulated spine. These observations are consistent with the first theoretical prediction.

Next, to better understand the origin of the AIP and FK506 mediated response change, we examined the temporal dynamics of CBP, $C(t)$ and $P(t)$ in the model (Fig. 2g). The cumulative sum of $P(t)$ in control and the two drug conditions helped us determine the fraction of P that underlie the spine plasticity (Fig. 2h). Interestingly, AIP substantially slowed $P(t)$ in association with stronger depression observed (Fig. 2g). Similarly, FK506 led to a stronger P response (Fig. 2h) by lowering the P-thresholds (cf. Fig. 2c), and consequently leading to additional potentiation. In both cases, the dynamics of $C(t)$ were largely unaffected. According to the model, this implies that the blockers have little to no effect on the CBP dynamics but affect the availability of P.

Differential heterosynaptic recruitment in the vicinity of multiple sLTP spines

Next, we turn to our second prediction that simultaneous sLTP events at multiple closely located spines will trigger the potentiation of neighbouring heterosynaptic spines due to an overlap in CBP. In the sLTP induction condition used in the present experiments, stimulation of a single spine has little effect on heterosynaptic spines (within $< 2\mu$m of the stimulated spines; see Fig. S1e and S1f). Whereas immediately after the stimulation, the heterosynaptic spines experience a small positive change, such a change is not sustained. Could the stimulation of multiple spines then be sufficiently strong to recruit heterosynaptic spines and induce longer-lasting plasticity in those non-stimulated spines? To explore this possibility, we simultaneously targeted three closely located spines for sLTP induction (encircled in blue, Fig. 3a; average distance of 4.5μm). We will denote all spines located between the activated spines as inside neighbour spines (I.N.) and those outside (but within 2 μm of

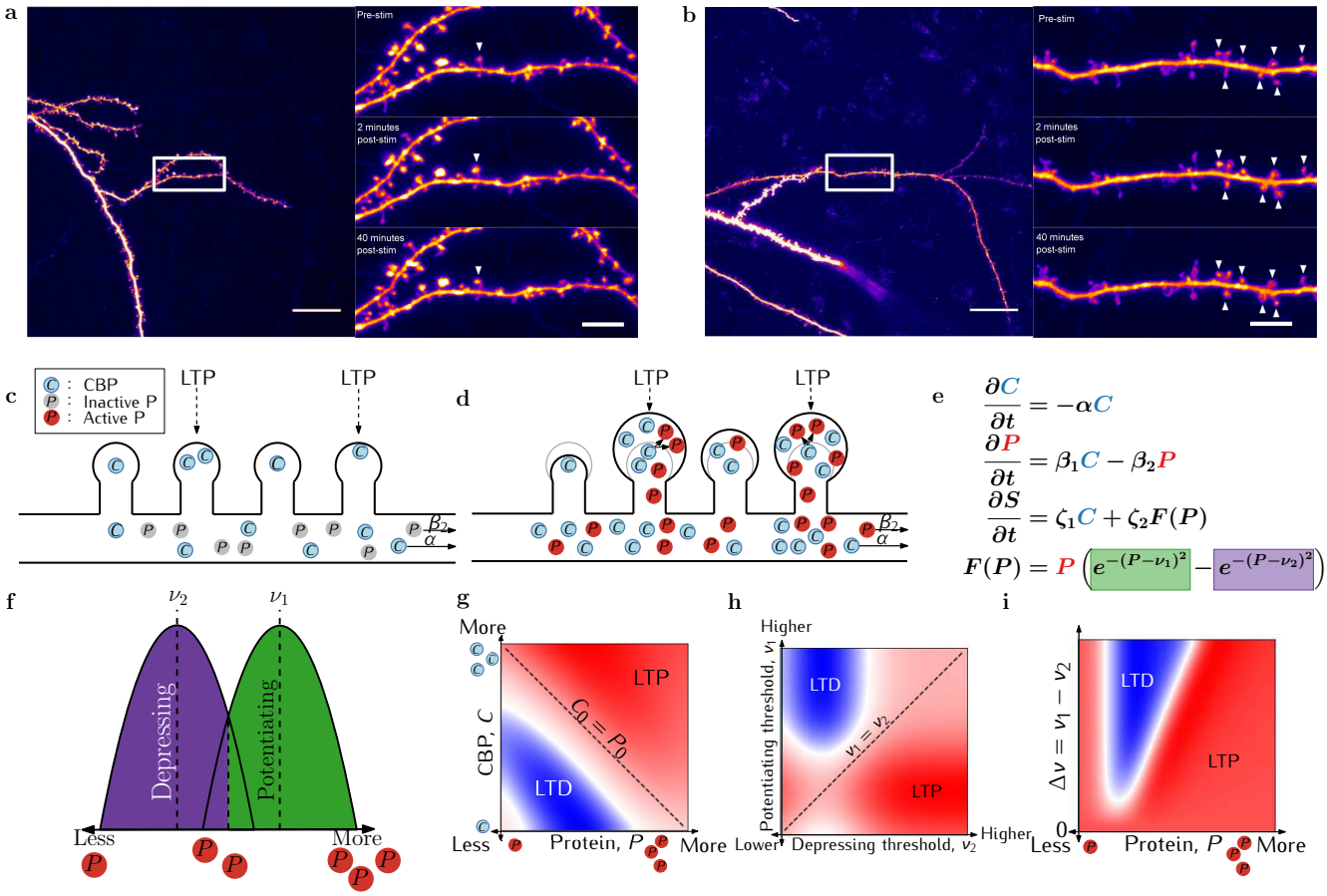

Figure 1: **Experimental outline as well as a sketch of the sLTP triggered spine dynamics along a dendrite and its model description.** **a)** GFP-expressing CA1 neuron used in a representative sLTP experiment targeting a single spine. **Left)** Apical oblique dendrite targeted for stimulation. Scale bar = 20μm. **Right)** Structural potentiation of a single dendritic spine (white arrow head). *Top*, before stimulation. *Middle*, 2 minutes post-stimulation. *Bottom*, 40 minutes post-stimulation. Scale bar = 5μm. **b)** GFP-expressing CA1 neuron used in a representative sLTP experiment targeting seven spines, simultaneously. **Left)** Apical oblique dendrite targeted for stimulation. Scale bar = 20μm. **Right)** Structural potentiation of a single dendritic spine (white arrow head). *Top*, before stimulation. *Middle*, 2 minutes post-stimulation. *Bottom*, 40 minutes post-stimulation. Scale bar = 5μm. **c)** Before sLTP induction, two CBP and P stores are available: at each spine and a shared pool in the dendrite. **d)** sLTP-triggered CBP increase activates the protein P which transitions with a rate β_1 from inactive to its active form. The activation of P together with CBP increase spine size. **e)** A computational model translating CBP and P concentrations into spine size, color code as in (a) and (b). **f)** Protein P can potentiate or depress spines, depending on $F(P)$. If P exceeds a threshold ν_1 a spine potentiates ($F(P) > 0$), if P drops below ν_2 a spine will reduce its size ($F(P) < 0$), the relative proximity to ν_1 and ν_2 governs size in the intermediate regime as shown here. **g)** Long-term potentiation (red) corresponds to a regime where either P or CBP are large while depression (blue) occurs when both P or CBP are low. Hereby, we kept all other model parameters constant, including the thresholds ν_1 and ν_2, and varied the initial concentrations C_0 (x-axis) and P_0 (y-axis). In **h)**, C_0 and P_0 where held constant while varying the potentiation and depression thresholds ν_1 and ν_2. In **i)**, C_0 and depression threshold ν_2 are kept fixed, while P_0 and the potentiation threshold, ν_1 are varied. On the x-axis we see the change in P_0, while the y-axis depicts the difference between the thresholds. The dashed horizontal line refers to the 0 point, i.e. $\nu_1 = \nu_2$. Below the dashed line the potentiation threshold is encountered first and vice versa for the area above the line. All three panels (g,h,i) show potentiation in red and depression in blue at $T = 40$ minutes post sLTP induction.

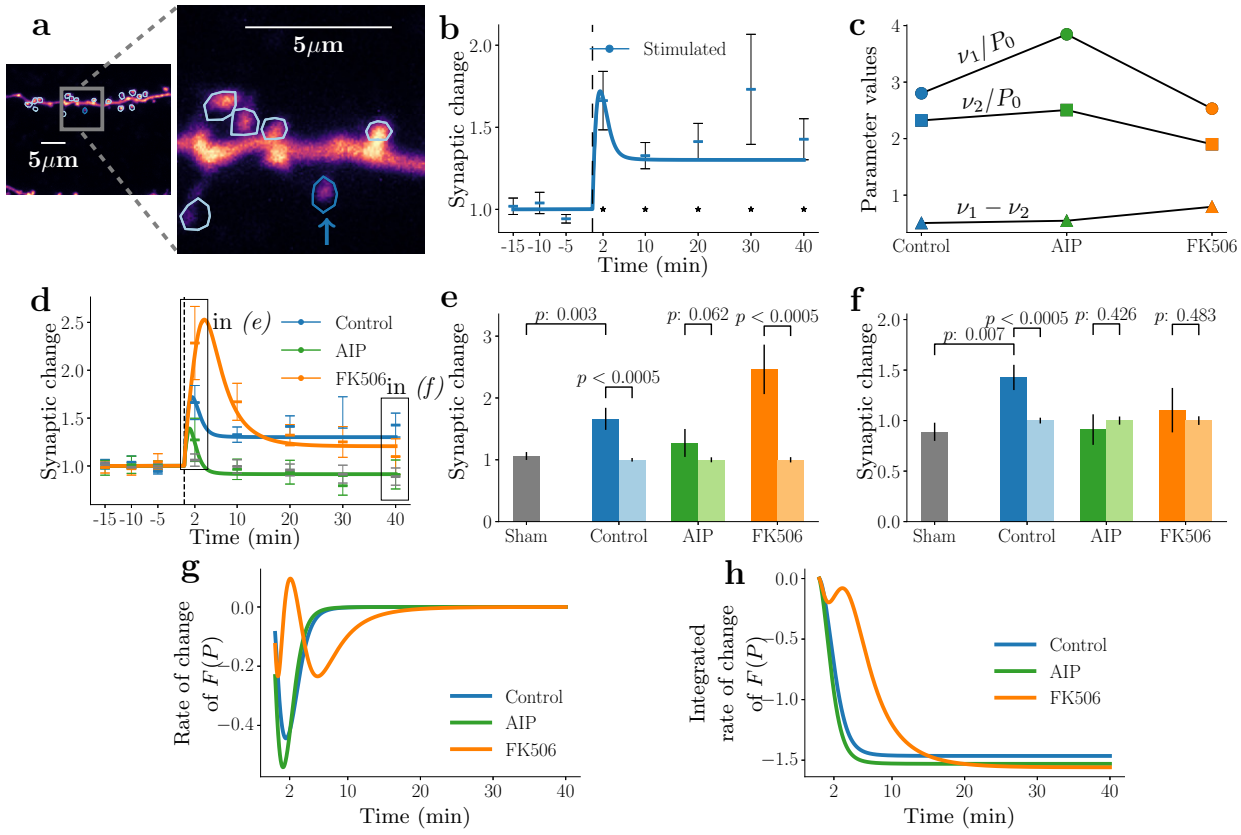

Figure 2: **sLTP at single spines occurs via an sLTP-mediated CBP increase. Reduction in Calcineurin (induced by FK506) lowers the potentiation threshold, and the blockage of CamKII (induced by AIP) raises it. a)** Dendritic anatomy during sLTP-induction at single spines. A dark blue ROI and arrow denote the stimulated spine. **b)** Spine averaged potentiation dynamics of activated spines recorded across 40 minutes, averaged across sLTP experiments and normalised to pre-sLTP baseline. Superimposed is a model fit (blue line), $*$ denotes $p < 0.05$ significance relative to sham. **c)** Calcineurin and CamKII and their blockers, AIP and FK506, respectively, control potentiation and depression threshold and the amount of activated protein P. **d)** Temporal dynamics of sLTP-induced potentiation in control conditions and in the presence of the CamKII and Calcineurin blockers. The lighter colours refer to the average response pre-stimulation. **e)** Normalised growth of all experimental conditions at $t = 2$ minutes post-sLTP (lighter bars represent the baseline before stimulation). **f)** Normalised growth of all experimental conditions at $t = 40$ minutes (lighter bars represent the baseline before stimulation). **g)** Temporal evolution of model parameter $F(P)$ derived from fits in (d) across control, AIP and FK506 conditions. **h)** Represents the associated cumulative dynamics.

the stimulated spines) as outside neighbour spines (O.N.). A plot of spine fluorescence change of the stimulated spines and the immediate neighbouring I.N. spines (encircled in white, Fig. 3a) as a function of time shows that simultaneous glutamate uncaging at three spines potentiates heterosynaptic I.N. spines at 2 min post-stimulation (Fig. 3b and 3d). In contrast, this heterosynaptic potentiation is not maintained over time and largely decays back to baseline (Fig. 3e). The transient potentiation of I.N. can be explained in the model by the dynamic shifts in the levels of P (Fig. 3c and 3f). We next sought to test the impact on stimulated, and I.N. spine plasticity of further increasing the number of spines stimulated for sLTP induction and analysing the experimental data with model fits. Upon stimulating seven spines, at 2 min post-stimulation, potentiation of heterosynaptic I.N. spines was still observed, whereas potentiation of targeted spines appeared slightly attenuated (Fig. 4b). Comparing the heterosynaptic I.N. response between three and seven homosynaptic spine stimulation (cf. light blue lines in Fig. 3b versus Fig. 4b), we find decreased potentiation amplitude in the heterosynaptic I.N. spines that are surrounded by seven rather than three stimulated spines. This indicates that heterosynaptic potentiation, at least for those spines within the stimulated spine cluster, is reduced as the number of simultaneously stimulated spines increases. Keeping this seven-spine stimulation condition, we studied the effects of AIP and FK506 on heterosynaptic I.N. spine plasticity similarly to the single spine stimulation case. First, taking a close look at the experimentally obtained responses of heterosynaptic I.N. spines, the extent potentiation at 2 min post-stimulation was increased by FK506 and reduced by AIP (Fig. 4e). Studying the changes in best fit model parameters across the heterosynaptic I.N. spine responses relative to those of stimulated spines (Fig. 4c), the level of P was lower at the heterosynaptic spines relative to their stimulated neighbours. The reduced P leads to a higher ν_2/P ratio that dampens the overall synaptic response because the synaptic dynamics are further away from the potentiation domain around ν_1. Moreover, a slight increase in the depressing threshold ν_2 (Fig. 4c) further contributes to the dampening of potentiation. We also note that the CBP level C_0 is decreased in the heterosynaptic I.N. spines relative to the stimulated spines, which could be explained by the spatial distance between the stimulated spines that is the Ca^{2+} source and the heterosynaptic spines where some diffusional loss of CBP is expected. A lower CBP level, in turn, decreases the level of P_0, which results in smaller potentiation amplitude at heterosynaptic spines. Upon considering the long-term changes, overall, both AIP and FK506 showed lasting effects on the stimulated and heterosynaptic spines. AIP decreased the short and long-term potentiation for both the stimulated and heterosynaptic I.N. spines. This effect could be explained in our model by a change in ratio $(\nu_1 - \nu_2)/P_0$ (Fig. 4f). FK506 led to a higher short and long-term potentiation for stimulated and heterosynapses. Interestingly, in the presence of FK506, no further increase in the average extent of potentiation of the stimulated spines was observed (Fig. 4d). In contrast, the heterosynaptic spines showed a larger degree of potentiation (Fig. 4e). This can be explained in our model by the limited availability of P at the directly stimulated spines due to the increase in the number of stimulated spines, and even with suppression of active calcineurin that counteracts potentiation, stimulated spines cannot recruit additional P to further potentiate inputs, which is otherwise possible when only one or three spines are stimulated (see Fig. 2 and Fig. 3). In contrast, the heterosynaptic I.N. spines are facilitated to undergo potentiation by recruiting a small amount of additional P when relieved of activity that counteracts potentiation by FK506.

Next, comparing single, three and seven spine stimulation paradigms, we sought to test the prediction of our model that, provided the distance between the stimulated spines is kept small, an increase in the number of stimulated spines should result in a larger potentiation due to accumulation of CBP and P. Consistent with the model, simultaneous potentiation of seven spines with an average inter spine distance of 2 μm ("clustered spines"; e.g. Fig. 4a) is larger than that of individually stimulated spines (Fig. 4i: see also Fig. 2b and Fig. 4b). This potentiation advantage disappears if the stimulated spines are spaced further apart with an average inter-spine distance of 6 μm ("distributed spines"). The effect of spatial confinement of simultaneously stimulated spines is summarised in Fig. 4i, where the potentiation for seven distributed spines is not significantly different from the single spine stimulation. Thus, more simultaneous and clustered sLTP events increase the size of early potentiation, which is consistent with the prediction, but only if they occur close in space and time. Our model provides a mechanistic framework for the spatial property of simultaneous sLTP induction: more simultaneous events within a confined area release more P due to the overlapping Ca^{2+} events and thus result in a stronger initial sLTP size (see Fig. 4g left). However, if the inter-spine distance grows, the spines will decouple because the spread of CBP and P from individual sLTP spines do not travel fast enough to influence each other or are attenuated before they can interact. Furthermore, in line with the model prediction, a comparison of the spine response following simultaneous stimulation of seven versus three spines (Fig. 3b) indicates that simultaneously triggering a larger number of clustered sLTP events leads to a smaller response at the stimulated

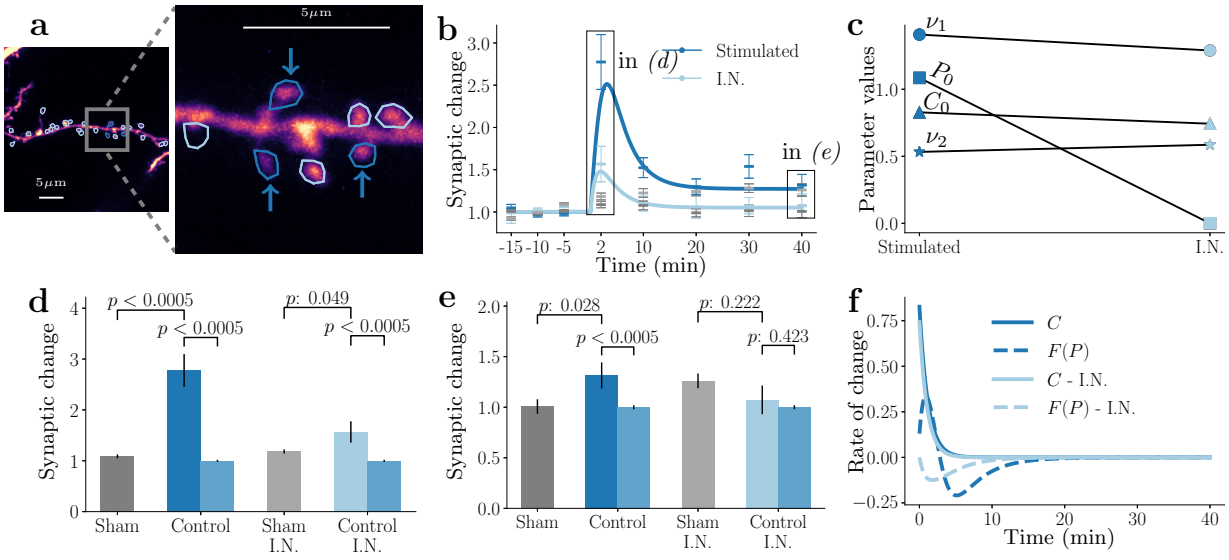

Figure 3: **sLTP in three spines is sufficient to co-potentiate immediate neighbours (I.N.), and the amount of potentiation can be explained by a spill-over of CBP from stimulated spines. a)** Sketch of sLTP induction at three neighbouring spines *in vitro*, including a zoom-in view. **b)** Normalised synaptic changes observed in the stimulated spines alongside changes in the neighbour spines and model fits. **c)** The difference in model parameters for the stimulated spines (stimulated) and immediate neighbours (I.N.). **d)** Normalized spine growth across experimental conditions at $t = 2$ minutes, immediately after simulation. $*$ refers to $p < 0.05$. **e)** normalised growth of all experimental conditions at $t = 40$ minutes. **f)** Dynamics of C and $F(P)$ given by the fitted model for the stimulated and inside neighbour spines. Insets represent the cumulative dynamics.

spines. Specifically, the extent potentiation of both the early and late phases is reduced when seven instead of three spines are stimulated. Such a result implies that the stimulated spines have passed a certain threshold where CBP and P are no longer available to support additional growth. In other words, the local competition for resources could place a ceiling on the degree of potentiation that spines undergo following synaptic activity.

Simultaneous glutamate uncaging at fifteen spines reveals strong competition and cooperation at the stimulated and heterosynaptic spines

Thus far, our model can reasonably predict the experimental results. Upon considering the cases for simultaneous stimulation of one, three and seven target spines, we observed that the fast potentiation component was the highest when three spines were simultaneously stimulated and declined in the case of seven spines (cf. Fig. 3, Fig. 4 and Fig. 6). In order to assess the robustness of the model and gain further insights into the dynamics of model parameters, we sought to push the envelope further and simultaneously potentiated fifteen closely located spines. We then monitored spine plasticity at the stimulated homosynaptic spines and their heterosynaptic neighbours. In particular, we wondered if the fast potentiation component declined further when fifteen spines were stimulated simultaneously and whether the parameters P_0 and C_0 at the stimulated and heterosynaptic spines could reveal a systematic dependence of initial C_0 on the number of stimulated spines. Fig. 5a illustrates a representative example of the layout of our new experiments. The fifteen stimulated spines (dark blue arrows) are located on a single dendritic branch and interspersed amongst the unstimulated heterosynaptic I.N. spines (encircled by light blue lines). The normalised spine fluorescence changes at the stimulated and heterosynaptic I.N. spines across time are shown in Fig. 5b. Compared to three and seven spine stimulation experiments, in both the stimulated and heterosynaptic I.N. spines, the extent potentiation at 2 min post-stimulation is reduced, whereas, at 40 min, the extent potentiation is maintained at a higher level (Fig. 5d and 5e). A plot of the model parameter values (Fig. 5c) illustrates that the initial C_0 is similar in the stimulated and the heterosynaptic I.N.

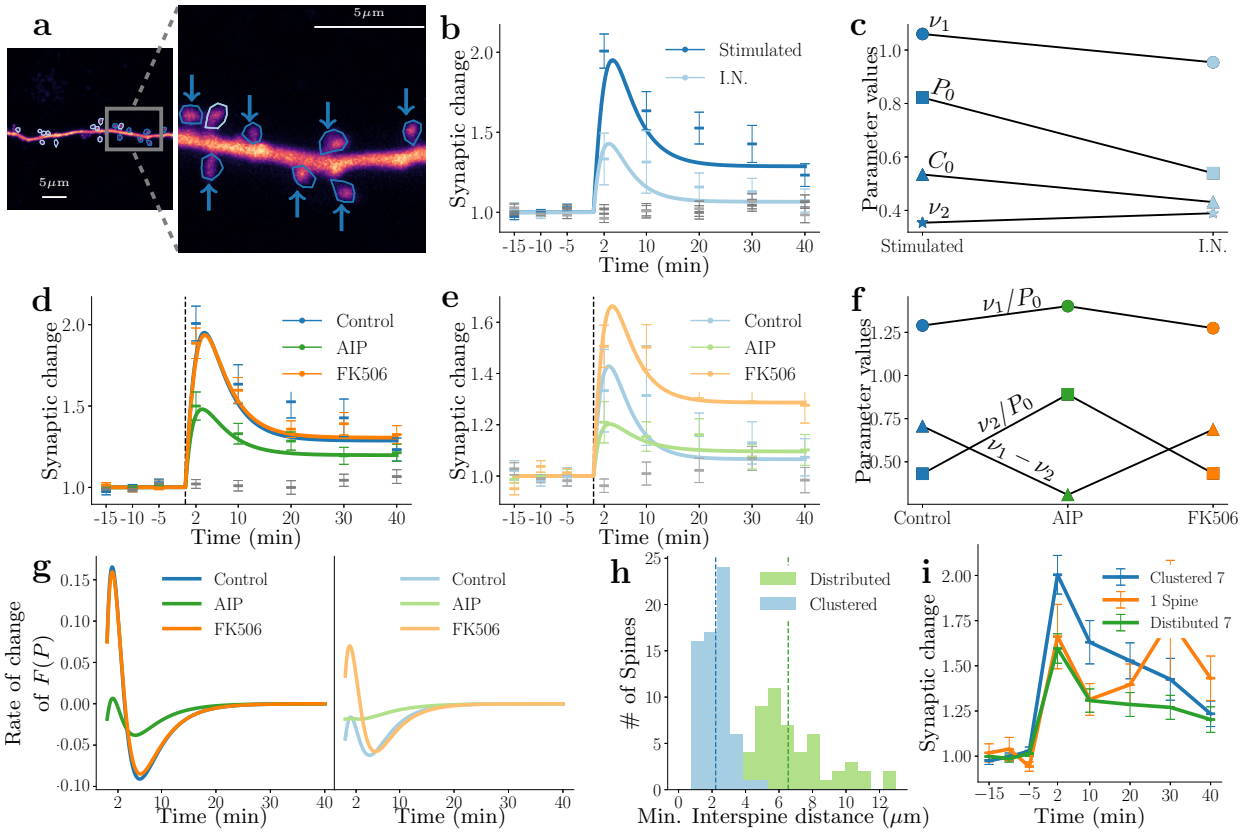

Figure 4: **Growing distance between spines and competition for resources leads to a lower sLTP response when seven spines are stimulated simultaneously. a)** Illustration of sLTP induction at seven spines with a zoomed-in view, arrows denote stimulated spines. **b)** Normalized spine changes in stimulated spines (dark blue) and inside neighbour spines (light blue), model fits are superimposed. **c)** Model parameters for stimulated and inside neighbour spines. **d)** Temporal dynamics of stimulated spines across drug conditions, model fits are superimposed. **e)** Temporal dynamics of immediate neighbour spines across drug conditions, model fits are superimposed. **f)** Changes in model parameters across drug conditions. **g)** Model dynamics of $F(P)$ in the stimulated (left) and the immediate neighbour spines (inside the stimulated cluster) (right) for the control, AIP and FK506 conditions, respectively. **h)** Distribution of the minimum inter-spine distance between stimulated spines, a quantity related to the size of the total cluster. **i)** Normalized spine changes of stimulated spines for the clustered seven spines (blue), distributed seven spines (green) and single spine (orange) experiments.

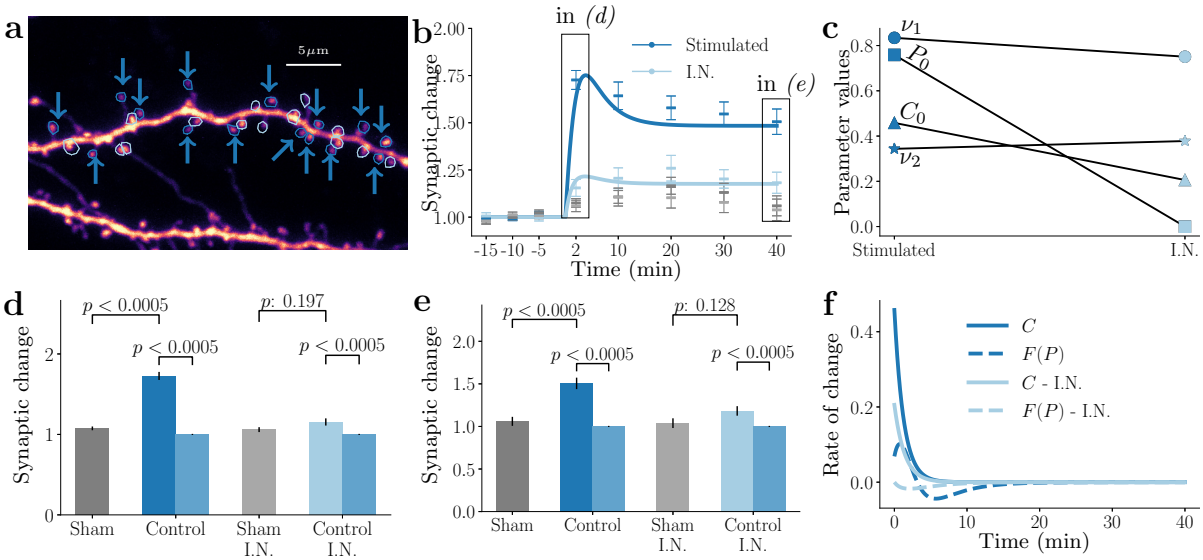

Figure 5: **Simultaneous induction of sLTP at fifteen spines reduces the amount of spine growth in the short time but increases spine strength for long time scales. a)** A visualization of the sLTP induction at fifteen spines: stimulated spines are denoted by a dark blue circle and an arrow, and ROIs of the unstimulated neighbouring spines are shown as light blue circles. **b)** Normalized synaptic changes in the stimulated spines (dark blue) and inside neighbour spines (light blue), model fits are superimposed. **c)** Model parameter differences across stimulated and inside neighbour spines. **d)** Normalized spine growth across all experimental conditions at $t = 2$ minutes, immediately after simulation. $*$ refers to $p < 0.05$ **e)** normalized spine growth at $t = 40$ minutes. **f)** Model dynamics of C and $F(P)$ in the stimulated and inside neighbour spines.

spines. However, the values of $C$and $F(P)$ are approximately half of the values observed in the experiments with three spines (cf. Fig. 3f). Interestingly, C_0 declines steadily from the three, seven, and fifteen spine experiments for the stimulated and heterosynaptic I.N. spines. From the three to the seven spine experiments, C_0 decreases by 36.4 percent and 42 percent for the stimulated and I.N. spines, respectively; from the seven to the fifteen spine experiments, C_0 decreases to 14.3 percent and 52.3 percent for the stimulated and I.N. spines, respectively. We will later take advantage of this drop to test for spine competition. The dynamics of P across spines show that the P_0 immediately after the start of the glutamate uncaging is elevated in the stimulated spines. However, the heterosynaptic spines do not profit from this increase, and their P_0 value is close to zero. This indicates that the heterosynaptic I.N. potentiation dynamics are initiated by the CBP spillover from stimulated spines, which in turn raises the local concentration of P to further potentiate the heterosynaptic I.N. spines. We interpret that a time delay for CBP-dependent accumulation of P to a level sufficient to support robust sLTP at I.N. spines contributes to the observed reduction of the early potentiation component at 2 min post-stimulation. However, once a stable level of P is achieved, P-driven sLTP that is predominant by 40 min is comparable in size to that observed for the stimulation of seven spines (see Fig. 4). Overall, these findings show that the number of spines simultaneously stimulated to undergo sLTP is a potent predictor of heterosynaptic potentiation at spines that share the dendritic locale: the more stimulated spines undergo sLTP, the more pronounced sLTP is also observed for heterosynaptic I.N. spines. Additionally, our model predicts that spine competition depletes the local stores of P and Ca^{2+} needed for spine potentiation and will therefore reduce the fast potentiation response at the simultaneously stimulated spines proportionally to the number of stimulated spines.

Comparing hetero- and homosynaptic potentiation across varying number of glutamate uncaging sites

Lastly, we summarise the spine plasticity dynamics across all our experiments. We simultaneously stimulated variable numbers of spines on a local dendritic branch and addressed the similarities and differences to help clarify the nature of underlying processes captured in our model. We have systematically compared C_0, P_0, and potentiation and depression thresholds ν_1 and ν_2, respectively, across one, three, seven or fifteen glutamate uncaging events. As discussed above, if the plasticity dynamics at the directly stimulated spines involve a shared pool of CBP and protein P, stimulating more spines could lead to competition in which C_0 and P_0 (i.e. the resources) assigned to each spine are reduced proportionally to the number of stimulated spines. We find that C_0 declines both for the directly stimulated and for the heterosynaptic I.N. spines, with the functional form $a/x+b$, where x is the number of simultaneous glutamate uncaging sites. Notably, the value of b is substantially larger for stimulated compared to heterosynaptic I.N. spines (Fig. 6a) and can be thought to be the spine inherent CBP released by sLTP. The level of P_0 in general is significantly higher in the stimulated spines, and it also follows the form $a/x + b$, where x is the number of simultaneous glutamate uncaging sites, and b is the constant amount of P accessible to the spines. For the heterosynaptic I.N. spines, the total dynamics of P are dominated by the spillover of C_0 and its action on P (Fig. 6b). In other words, since the initial value, P_0 at the heterosynaptic I.N. spines is small and fluctuates across experiments while the level of C_0 is comparable in size to that of the stimulated spines (Fig. 6a), C_0 is a plausible source for shaping the potentiation of the heterosynaptic I.N. spines. Interestingly, ν_1 and ν_2 decline also in a manner that is inversely proportional to the number of stimulated spines (Fig. 6c,d). This suggests that the spines could lower their potentiation and depression thresholds to offset the increasingly limited resources and promote potentiation. Notably, in order to aim for a valid model across the full dendrite with the model parameters between stimulated and heterosynaptic I.N. spines being comparable, the potentiation and depressing thresholds, ν_1 and ν_2 of the stimulated spines were used to obtain the heterosynaptic dynamics.

That the dependence of C_0, P_0, and ν_1 and ν_2, follows the functional form $a/x + b$ as described above indicates that the resources available for potentiation are divided among the potentiating spines. However, do the available resources stay constant across experiments with a varying number of uncaging sites or do spines cooperate to generate more resources that are then shared among all potentiating spines? To address this question, we have studied the sum total of the changes in the size of spines along the dendritic locale of stimulated spines within the field of view, including those of the stimulated spines themselves. We find that the total area increases linearly with the number of stimulated spines (Fig. 6e). If spines were only competing for a finite and constant resource, we would have expected an approximately constant integrated spine area. The linear growth proportional to the number of uncaging events could suggest the recruitment of additional

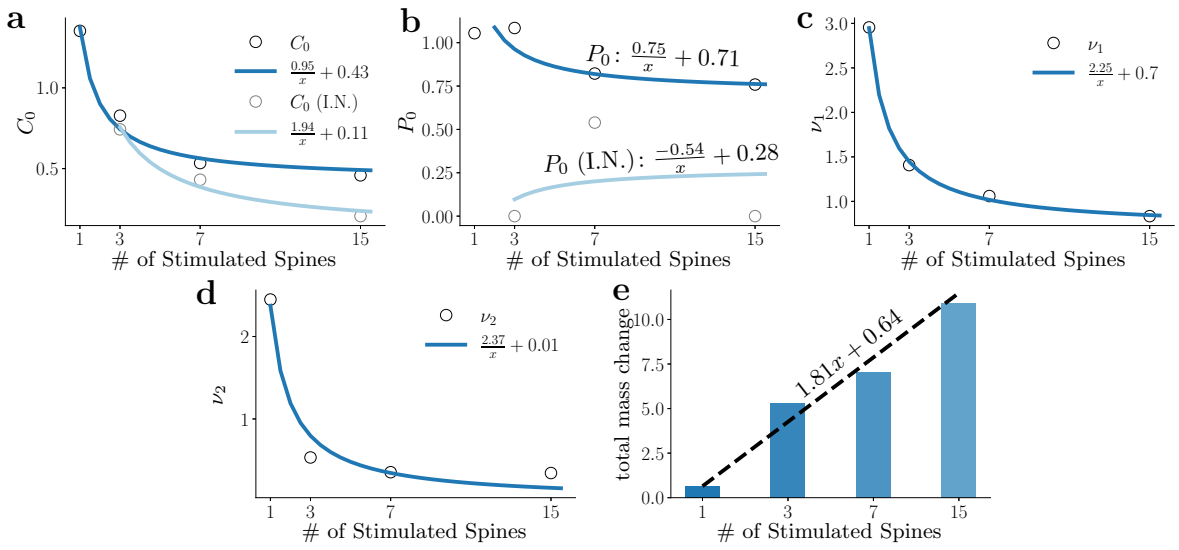

Figure 6: **A mix of spine competition and cooperation revealed by a varying number of simultaneous sLTP events. a)** Decline in the baseline amount of CBP, C_0, is inversely proportional to the number of induced sLTP events (1/# stimulated spines) both in the stimulated spines (dark blue) and in the inside neighbour spines (light blue), demonstrating a competition for resources across spines. **b)** Decline in the baseline amount of protein P_0 in the stimulated and inside neighbour spines is also inversely proportional to the number of sLTP events (# stimulated spines). **c, d)** Decline in the potentiation threshold (c) and in the depression threshold (d) is inversely proportional to the number of sLTP events (# stimulated spines) in the stimulated spines and their inside neighbour spines. **e)** Total synaptic growth integral (integrated across all stimulated spines of an experiment relative to baseline) vs # stimulated spines demonstrates a cooperative increase in synaptic strength even though sLTP amplitude at the individual sLTP spines declines as a function of # stimulated spines, see Fig. S1.

resources, for example, a collaborative activation of additional CBP stores that allows the spines to potentiate.

Discussion

Previous work exploring heterosynaptic dynamics on single dendrites has demonstrated a mixture of compensatory and non-compensatory forms of plasticity, dependent on the stimulation, ages, and cell type (Engert and Bonhoeffer, 1997; Govindarajan et al., 2011; Tong et al., 2021) and has typically employed a single stimulation intensity to induce homosynaptic plasticity. Here we systematically varied the number of targeted inputs from 1 to 15 spines and both directly imaged and modelled the impact of triggering sLTP on homosynaptic and heterosynaptic spine plasticity. We find that simultaneous homosynaptic potentiation of clusters of inputs leads to the spreading of plasticity to nearby spines. Upon stimulating a higher number of homosynaptic inputs, compensatory mechanisms begin to limit the magnitude of potentiation. Moreover, our model correctly predicts how the available CBP and protein P necessary for promoting potentiation within the local dendritic vicinity are shared between inputs, leading to the changes in spine structure.

Relation to previous studies

Clustered stimulation

Previous studies have employed similar experimental techniques to explore heterosynaptic interactions on single stretches of dendrites (Harvey and Svoboda, 2007; Govindarajan et al., 2011; Oh et al., 2015; Tong et al., 2021) but showed a variety of seemingly incompatible plasticity outcomes that can be understood using insights from our model. Many prior sLTP studies using glutamate uncaging have involved potentiating a single isolated spine on a dendrite, thereby likely minimizing the impact on heterosynaptic inputs (for example Matsuzaki et al. (2004); Harvey and Svoboda (2007)). We consistently find no significant heterosynaptic dynamics when we target a single spine to elicit potentiation. On the other hand, a small group of studies have employed multiple spine uncaging on dendritic segments. For example, in the case of Oh et al. (2015), eliciting LTP in a group of clustered spines resulted in heterosynaptic depression of an unstimulated spine inside the cluster, which was dependent on calcineurin activity. Whereas this finding differs from our current result, where we see potentiation of inside cluster spines, the apparent disagreement can be explained by differences in stimulation paradigms. Oh et al. (2015) stimulated each LTP spine on its own, one by one, in turn, a condition which is unlikely to generate a substantial dendritic calcium transient. Moreover, the time taken to complete stimulating all the targeted spines would have been longer (at least 6 min) than the 60 sec in the current study. Such a major difference in the activity pattern likely engages different endogenous dendritic mechanisms. Govindarajan et al. (2011) stimulated groups of spines either on a single dendrite or across a pair of dendritic branches and measured the dependence of homosynaptic sLTP on a local supply of freshly translated protein. In this study, the strength, frequency, and number of pulses received by each homosynaptic spine were varied between the single spine condition and the multiple spine condition, unlike in the current study where the glutamate uncaging stimulation condition for each target was kept constant irrespectively of the number of spines stimulated. Finally, previous work from Tong et al. (2021) has demonstrated a mixture of heterosynaptic potentiation and depression following the simultaneous potentiation of groups of spines on single dendritic branches (Tong et al., 2021). Again, here, the differences in stimulation parameters may explain differences in the measured outcome. Tong et al. (2021) used a whole-cell patch-clamp to depolarize the postsynaptic neuron to 0mV for one minute to promote NMDAR activation whilst uncaging glutamate onto the homosynaptic spines, to elicit structural plasticity. This likely initiated broader and more extensive signalling in the dendrite/neuron, whereas in the current study, the experiments were performed in nominally magnesium-free aCSF without deliberate depolarization of the postsynaptic cell membrane. It is unclear which protocol best represents the *in vivo* condition where it is highly likely that multiple inputs may be synchronously active on a single dendrite during behaviour and, in turn, require the postsynaptic machinery to recognize this local spatio-temporal synchrony and respond accordingly. Regardless, our study is an attempt to identify the minimal components of molecular signalling machinery that can represent the behaviour of active and inactive spines along stretches of dendrites.

Local versus global effects

On the spatial and temporal scales investigated, we find that the spines sharing a short region of dendrite appear not to be competing for a limited resource (Figure 6e). However, this result does not rule out changes that may be occurring elsewhere in the neuron, outside the imaging ROI, nor can it account for plasticity events that may act to rebalance the network on longer timescales than explored here. Presumably, the clustered potentiation induced in these experiments must have upper limits (as demonstrated in the 15 spine condition, see figure 5), and homeostatic mechanisms that act to normalize neuronal activity levels (such as synaptic scaling of AMPARs) may operate over slower timescales to be monitored in the current study. Following these dendrites on longer timescales (hours to days) may reveal additional patterns of homosynaptic- and heterosynaptic plasticity that are not apparent here.

Additionally, regarding the sum total growth of estimated spine volumes, we have observed (see figure 6e), we note that we cannot exclude local synthesis of proteins occurring. The results that we obtained within the studied spatial and temporal scales are consistent with other studies. This effect may require additional consideration in revising the model for a future study as the total stores that are shared among spines may not be constant in time or space as is assumed here.

Presynaptic identity

Our current study has focused entirely on monitoring dendritic spine strength using the intensity of a fluorescent protein (GFP) as a readout. This is a well-used and validated approach, both *in vitro* and *in vivo*, and for example, has been used to demonstrate sLTP associated with behavioural task acquisition (Matsuzaki et al., 2004; Hayashi-Takagi et al., 2015). Single-cell expression of the fluorophore allows excellent signal-to-noise readout of GFP spine signals and the ease of imaging of large populations of inputs over time. However, the method does not give information about the presynaptic identity of the axons arriving onto the spines. Our study used apical oblique dendrites of CA1 neurons, and thus the incoming axons are likely part of the Schaffer collaterals originating in CA3. These inputs have been shown to make multiple contacts onto single CA1 neurons (Druckmann et al., 2014) including onto single dendritic branches. It would be of interest to determine the plasticity rules when a cluster of dendritic spines sharing the same presynaptic input is potentiated and how well such rules are matched to spine behaviour following plasticity induction with synchronous glutamate uncaging that bypasses communication with the presynaptic terminals. In our study, glutamate uncaging of smaller cluster sizes (3 and 7 spines) could reflect a single input, or a pair of inputs, being potentiated together. Further work is required to determine if individual inputs are somehow recognized and privileged from a postsynaptic point of view.

Computational models of heterosynaptic effects

With the introduction of the protein P, our model aims to retain the essence of the calcium amplitude hypothesis, which states that the peak calcium determines the direction of plasticity (either sLTP or sLTD) (Evans and Blackwell, 2015). While our model does not directly include a calcium term, the model indirectly accounts for calcium changes through the CBP variable, which drives the P dynamics. Specifically, instead of calcium, a low P elevation results in sLTD, while a higher elevation results in sLTP in our model.

Experimental studies that motivate this hypothesis include the work by Artola et al. (1990) showing that post-synaptic depolarization level could affect the direction of plasticity while the stimulation frequency was kept constant. Cho et al. (2001) showed that directly lowering the extracellular calcium concentration turned sLTP into sLTD. In addition, using intracellular uncaging of calcium, (Yang et al., 1999) reported that a brief but high elevation of calcium resulted in sLTP, whereas a longer but a small rise in calcium triggered sLTD. To simulate this effect, several models have been proposed that manipulate the calcium amplitude and evaluate either frequency-based (Artola et al., 1990; Hansel et al., 1996), STDP-based plasticity rules (for a review see Graupner and Brunel (2010)) or both (Shouval et al., 2002; Bush and Jin, 2012; Helias et al., 2008). Several important predictions have arisen from these models, including the supralinear relationship between stimulation frequency and calcium amplitude (Gamble and Koch, 1987) or Shouval et al. (2002) whose model was able to fit the frequency-based plasticity curve and partly match a spike timing (STDP) based plasticity response. Finally, using a stochastic transition approach between high and low synaptic states (Bush and Jin, 2012) were able to predict frequency-dependent plasticity but matched the observed plasticity due to a variety of other induction

protocols such as subthreshold depolarizations and burst pairings. However, studies have also demonstrated that relying solely on calcium amplitude will always lead to discrepancies with experimental results, e.g.Rubin et al. (2005), showed that any such pure calcium-threshold model will always exhibit a second sLTD window at long positive timing intervals, which are not observed in experiments. Furthermore, work done by Nevian and Sakmann (2006) observed that the calcium amplitude could predict sLTP and sLTD of the spine at extreme concentrations, but there is a middle-range where calcium amplitude does not predict the direction of plasticity. Other, more recent models looking beyond the calcium amplitude hypothesis include work by Ebner et al. (2019) that modelled cooperative plasticity exists across the dendritic tree as well as within single branches on a scale of milliseconds, and Triesch et al. (2018) that used a finite pool of receptors to show a variety of heterosynaptic behaviours as a consequence of competitive effects.

Biological candidates of P and CBP

Up to this point, we have not speculated on the exact nature of both the CBPs and P. However, several candidates have been previously studied that might represent these quantities. We stress that CBPs and P may not necessarily be restricted to single proteins but may represent a group of proteins that act collectively to achieve the results seen in the experiments.

In our experiments, we have presented results pertaining to the inhibition of calcineurin and CaMKII. Calcineurin inhibition has previously been seen to prevent heterosynaptic sLTD without affecting homosynaptic sLTP within a spatial extent of 4μm of the activation site (Oh et al., 2015; Tong et al., 2021), whilst inhibition of CaMKII leads to deficits in sLTP (Silva et al., 1992) and heterosynaptic sLTP (Tong et al., 2021). Other candidate molecules for P include Inositol trisphosphate receptors (IP3Rs) which have a similar effect on heterosynaptic sLTP as calcineurin Oh et al. (2015), h-Ras which has been seen to lower the threshold for neighbouring spine sLTP induction (Harvey et al., 2008) or RhoA which, following synaptic activity, exits the spine and diffuses along the dendrite (Murakoshi et al., 2011).

Candidates for CBP include, naturally, Ca^{2+} which has been strongly implicated in synaptic plasticity (Evans and Blackwell, 2015), the ARC gene product, which acts in the form of slow homosynaptic sLTP followed by heterosynaptic sLTD (El-Boustani et al., 2018) or NO synthase that produces Nitric Oxide, which in turn facilitates sLTP in one neuron and then spreads to neighbouring neurons to affect synaptic strength (Schuman and Madison, 1994; Padamsey et al., 2017).

Designing experiments with these quantities in mind could reveal more about the nature and composition of both the CBP and P.

The contribution of the model

Throughout this work, we have introduced a model that uses the protein P as the primary driver of the dual sLTP and sLTP nature of plasticity. Thus, we can capture diverse experimental outcomes across different spatio-temporal combinations of induction sites while retaining the basic features of homo- and heterosynaptic plasticity. Our model, which is continuous in time, allows for a study of both short-term and long-term saturation effects of plasticity, as is observed by the parameter fits for the experimental results across different experimental conditions. Interestingly, our model could predict the experimentally observed spine change across different experimental conditions using only two dynamic variables, CBP and P. This will allow it to be employed in spiking network simulations and, thus, give insight into the circuit-level consequences of the observed heterosynaptic plasticity rules.

Methods

Experimental

Preparation of organotypic hippocampal slice culture

Organotypic hippocampal slices were prepared as previously reported (Stoppini et al., 1991). Briefly, hippocampi of postnatal day P6-7 Wistar rat pups (Nihon SLC) were isolated and cut into 350 mm-thick transverse slices on a McIlwain tissue chopper (Mickle Laboratory Engineering Co. sLTD. and Cavey Laboratory Engineering

Co. sLTD.). Slices were transferred onto cell culture inserts (0.4 mm pore size, Merck Millipore) and placed in a 6-well plate filled with 1 ml/well of culture media containing 50% Minimum Essential Medium (MEM, Thermo Fisher Scientific), 23% EBSS, 25% horse serum (Thermo Fisher Scientific), and 36 mM glucose. Slices were maintained at 35°C and 5% CO_2 and used for experiments at DIV14-18. During experiments, slices were constantly perfused (1-2 ml/min) with artificial cerebrospinal fluid (aCSF) containing (in mM) 125 NaCl, 2.5 KCl, 26 $NaHCO_3$, 1.25 NaH_2PO_4, 20 glucose, 2 $CaCl_2$ and 4mM MNI-glutamate (Tocris). aCSF was continually bubbled with 95%O_2, and 5%CO_2 and experiments were carried out at room temperature. For a subset of experiments, calcineurin or CaMKII was inhibited with FK506 (2μM, Tocris) or myristolated Autocamtide-2-related inhibitory peptide (AIP, 5μM, Calbiochem) respectively. All animal experiments were approved by the RIKEN Animal Experiments Committee and performed in accordance with the RIKEN rules and guidelines. Animal Experiment Plan Approval no. W2021-2-015(3).

Transfection and imaging of CA1 pyramidal neurons

Organotypic slices were biolistically transfected using a Helios gene gun and used for experiments 48-96hrs later. For structural plasticity experiments, gold particles were coated in a plasmid encoding EGFP. 50μg of EGFP plasmid were coated onto 20-30mg of 1.6μm gold particles. Neurons were imaged at 910nm on a Zeiss 780 microscope, and all data was analysed offline.

Dendritic spine imaging and glutamate photolysis

Regions of dendrites were chosen by eye for imaging and stimulation. Regions were imaged for a brief baseline period by collecting z stacks of the dendritic arbour (512×512, 4× digital zoom for a final frame size of 33.7μm). The z step was 0.5μm. Glutamate was uncaged onto spines lying in the focal z plane using custom-written software at a distance of 0.5μm from the spine head. MNI-glutamate was photolyzed with a 2-photon laser source (720 nm), and each dendritic spine received a train of 60 pulses of laser light, each 4msec long, repeated at 1Hz. For sham experiments, MNI-glutamate was omitted from the aCSF. For groups of stimulated spines, laser pulses were delivered in a pseudo-simultaneous fashion, in which the first spine receives a pulse of glutamate (4msec), which is followed by a short delay (<3msec) as the system moves the laser to the next spine. This is repeated for all spines in the stimulated cluster (3, 7, or 15) and repeated at 1Hz.

Numerical

Image Analysis

Estimated spine volumes were obtained from background-subtracted maximum-projected fluorescence images using the integrated pixel intensity (see (Chen et al., 2015; Bartol Jr et al., 2015)) of an octagonally shaped ROI surrounding the spine head. These values were normalized against the three observed data points immediately preceding the glutamate uncaging. The spine ROI was generated by using a semi-automatic in-house python package that took advantage of the structures of the spines (see the appendix for a full list and description) to generate a reproducible ROI. The manual interaction involves a simple clicking on the interior of the spines while the ROI and subsequent measurement are performed automatically. Temporal shifting was corrected by using a phase cross-correlation algorithm implemented in SciPy (Guizar-Sicairos et al., 2008). The entirety of this algorithm is designed and written in a user-friendly python package available for download. Synapses that were partially obscured by the dendrite or overlapped with other spines were omitted in the analysis. A significance test determined the success of an experiment in the form of a z-test, with less than 15% of experiments considered failures. All images shown are maximum intensity projects of the 3D stacks.

Statistical definitions

Once the spines' luminosities were normalised against their baseline, they were pooled across experiments. All statistics were calculated with this dataset. Error bars represent the standard error of the mean, and significance was set at $p = 0.05$ (studentised bootstrap). Single asterisks indicate $p < 0.05$.

Model fitting algorithm

The values of the parameters $P_0, C_0, \alpha, \beta_{1,2}, \zeta_{1,2}$ and $\nu_{1,2}$ of the model (see the equation in figure Fig. 1f)) were obtained using a non-linear least-squares approach. The fitting routine included the introduction of a cost function that, when minimised, enforces agreement between the simulated model and observed data points and an iterative update scheme that finds parameters that best represent the experimental data. Mathematically, the cost function can be defined as

$$\sum_{t=0}^{T}(S - \hat{L}_i)^2 dt \tag{5}$$

where T is the length of the experiment (in our case, 40 minutes) and L_i refers to the averaged response of the spine of type i (which can be the stimulated or inside neighbour spines). We note, however, that the experimental snapshots are discrete in time and the above formulation is continuous. Thus, the cost functional needs to be rewritten to reflect the discontinuity as follows

$$\sum_{t=0}^{T}(S(t,x) - \hat{L}_{x,t})^2 \tag{6}$$

where $\hat{L}_{i,t}$ is the spine response at snapshot t. The iterative scheme we chose to employ is a gradient-based adjoint approach (Jameson (1988) or Skene et al. (2021)). The adjoint method was chosen, in part, due to its ability to easily and efficiently handle multiple simultaneous optimisation parameters. A numerical solution, implemented in a python code and available on request, supported the optimisation routine to provide feedback on the model dynamics given a set of parameters. The initial parameter fits were obtained with the values obtained from the three spine paradigm. The quantities that we considered independent across experimental set-ups ($\alpha, \beta_{1,2}, \zeta_{1,2}$) were frozen. The other control paradigms were obtained by altering the initial amount of C and P as well as the P thresholds ($\nu_{1,2}$). These values were similarly fitted in the multi-spine experiments to understand the dynamics of the heterosynaptic spines. Finally, for the experiments where CamKII and Calcineurin blockers were present, only the initial P and thresholds were changed. We note that the sham experiments were fitted by setting the initial C_0 and P_0 (values inherent to the stimulation process) to 0. For each optimisation, the convergence of obtained parameter fits was ensured by initiating the routine ten separate times with randomly chosen initial parameter configurations.

Data and code availability

Experimental data sets included in the manuscript and the computer code underlying this study can be found in this public github repository https://github.com/meggl23/MultiSpinePlasticity.

Acknowledgements

This research was supported by University of Bonn Medical Center, University of Mainz Medical Center, ReALity program at the Mainz Medical Center, RIKEN Center for Brain Science, JSPS Core-to-Core Program (JPJSCCA20220007 to YG), the European Research Council ('MolDynForSyn' Grant Agreement no. 945700) (TT), and by an add-on fellowship of the Joachim Herz Stiftung (ME). TT and YG thank all our group members for fruitful discussions, Janko Petkovic for feedback on an earlier version of the manuscript (TT).

References

Alain Artola, S Bröcher, and Wolf Singer. Different voltage-dependent thresholds for inducing long-term depression and long-term potentiation in slices of rat visual cortex. *Nature*, 347(6288):69–72, 1990.

Thomas M Bartol Jr, Cailey Bromer, Justin Kinney, Michael A Chirillo, Jennifer N Bourne, Kristen M Harris, and Terrence J Sejnowski. Nanoconnectomic upper bound on the variability of synaptic plasticity. *Elife*, 4: e10778, 2015.

Tiago Branco and Michael Häusser. Synaptic integration gradients in single cortical pyramidal cell dendrites. *Neuron*, 69(5):885–892, 2011.

Daniel Bush and Yaochu Jin. Calcium control of triphasic hippocampal stdp. *Journal of computational neuroscience*, 33(3):495–514, 2012.

Pico Caroni, Flavio Donato, and Dominique Muller. Structural plasticity upon learning: regulation and functions. *Nature Reviews Neuroscience*, 13(7):478–490, 2012.

Thomas E Chater and Yukiko Goda. My neighbour hetero—deconstructing the mechanisms underlying heterosynaptic plasticity. *Current Opinion in Neurobiology*, 67:106–114, 2021.

Xiaobing Chen, Jonathan M Levy, Austin Hou, Christine Winters, Rita Azzam, Alioscka A Sousa, Richard D Leapman, Roger A Nicoll, and Thomas S Reese. Psd-95 family maguks are essential for anchoring ampa and nmda receptor complexes at the postsynaptic density. *Proceedings of the National Academy of Sciences*, 112 (50):E6983–E6992, 2015.

Marina E Chicurel and Kristen M Harris. Three-dimensional analysis of the structure and composition of ca3 branched dendritic spines and their synaptic relationships with mossy fiber boutons in the rat hippocampus. *Journal of comparative neurology*, 325(2):169–182, 1992.

K Cho, John Patrick Aggleton, MW Brown, and ZI Bashir. An experimental test of the role of postsynaptic calcium levels in determining synaptic strength using perirhinal cortex of rat. *The Journal of physiology*, 532 (2):459–466, 2001.

Shaul Druckmann, Linqing Feng, Bokyoung Lee, Chaehyun Yook, Ting Zhao, Jeffrey C Magee, and Jinhyun Kim. Structured synaptic connectivity between hippocampal regions. *Neuron*, 81(3):629–640, 2014.

Francis J Dumont. Fk506, an immunosuppressant targeting calcineurin function. *Current medicinal chemistry*, 7(7):731–748, 2000.

Christian Ebner, Claudia Clopath, Peter Jedlicka, and Hermann Cuntz. Unifying long-term plasticity rules for excitatory synapses by modeling dendrites of cortical pyramidal neurons. *Cell reports*, 29(13):4295–4307, 2019.

Sami El-Boustani, Jacque PK Ip, Vincent Breton-Provencher, Graham W Knott, Hiroyuki Okuno, Haruhiko Bito, and Mriganka Sur. Locally coordinated synaptic plasticity of visual cortex neurons in vivo. *Science*, 360(6395):1349–1354, 2018.

Florian Engert and Tobias Bonhoeffer. Synapse specificity of long-term potentiation breaks down at short distances. *Nature*, 388(6639):279–284, 1997.

RC Evans and KT Blackwell. Calcium: amplitude, duration, or location? *The Biological Bulletin*, 228(1):75–83, 2015.

Reiko Maki Fitzsimonds, Hong-jun Song, and Mu-ming Poo. Propagation of activity-dependent synaptic depression in simple neural networks. *Nature*, 388(6641):439–448, 1997.

Min Fu, Xinzhu Yu, Ju Lu, and Yi Zuo. Repetitive motor learning induces coordinated formation of clustered dendritic spines in vivo. *Nature*, 483(7387):92–95, 2012.

Hajime Fujii, Masatoshi Inoue, Hiroyuki Okuno, Yoshikazu Sano, Sayaka Takemoto-Kimura, Kazuo Kitamura, Masanobu Kano, and Haruhiko Bito. Nonlinear decoding and asymmetric representation of neuronal input information by camkiiα and calcineurin. *Cell reports*, 3(4):978–987, 2013.

Edward Gamble and Christof Koch. The dynamics of free calcium in dendritic spines in response to repetitive synaptic input. *Science*, 236(4806):1311–1315, 1987.

S Glazewski, KP Giese, A Silva, and K Fox. The role of α-camkii autophosphorylation in neocortical experience-dependent plasticity. *Nature neuroscience*, 3(9):911–918, 2000.

Arvind Govindarajan, Raymond J Kelleher, and Susumu Tonegawa. A clustered plasticity model of long-term memory engrams. *Nature Reviews Neuroscience*, 7(7):575–583, 2006.

Arvind Govindarajan, Inbal Israely, Shu-Ying Huang, and Susumu Tonegawa. The dendritic branch is the preferred integrative unit for protein synthesis-dependent ltp. *Neuron*, 69(1):132–146, 2011.

Michael Graupner and Nicolas Brunel. Mechanisms of induction and maintenance of spike-timing dependent plasticity in biophysical synapse models. *Frontiers in computational neuroscience*, 4:136, 2010.

Manuel Guizar-Sicairos, Samuel T Thurman, and James R Fienup. Efficient subpixel image registration algorithms. *Optics letters*, 33(2):156–158, 2008.

C Hansel, A Artola, and W Singer. Different threshold levels of postsynaptic [ca2+] i have to be reached to induce ltp and ltd in neocortical pyramidal cells. *Journal of Physiology-Paris*, 90(5-6):317–319, 1996.

Christopher D Harvey and Karel Svoboda. Locally dynamic synaptic learning rules in pyramidal neuron dendrites. *Nature*, 450(7173):1195–1200, 2007.

Christopher D Harvey, Ryohei Yasuda, Haining Zhong, and Karel Svoboda. The spread of ras activity triggered by activation of a single dendritic spine. *Science*, 321(5885):136–140, 2008.

Akiko Hayashi-Takagi, Sho Yagishita, Mayumi Nakamura, Fukutoshi Shirai, Yi I Wu, Amanda L Loshbaugh, Brian Kuhlman, Klaus M Hahn, and Haruo Kasai. Labelling and optical erasure of synaptic memory traces in the motor cortex. *Nature*, 525(7569):333–338, 2015.

Moritz Helias, Stefan Rotter, Marc-Oliver Gewaltig, and Markus Diesmann. Structural plasticity controlled by calcium based correlation detection. *Frontiers in Computational Neuroscience*, 2:7, 2008.

Takao K Hensch. Critical period plasticity in local cortical circuits. *Nature Reviews Neuroscience*, 6(11):877–888, 2005.

Kai Hormann and Alexander Agathos. The point in polygon problem for arbitrary polygons. *Computational geometry*, 20(3):131–144, 2001.

Atsuhiko Ishida, Isamu Kameshita, Sachiko Okuno, Takako Kitani, and Hitoshi Fujisawa. A novel highly specific and potent inhibitor of calmodulin-dependent protein kinase ii. *Biochemical and biophysical research communications*, 212(3):806–812, 1995.

David B Jaffe, Daniel Johnston, Nechama Lasser-Ross, John E Lisman, Hiroyoshi Miyakawa, and William N Ross. The spread of na+ spikes determines the pattern of dendritic ca2+ entry into hippocampal neurons. *Nature*, 357(6375):244–246, 1992.

A. Jameson. Aerodynamic design via control theory. *J. Sci. Comp.*, 3(3):233–260, 1988.

Narayanan Kasthuri, Kenneth Jeffrey Hayworth, Daniel Raimund Berger, Richard Lee Schalek, José Angel Conchello, Seymour Knowles-Barley, Dongil Lee, Amelio Vázquez-Reina, Verena Kaynig, Thouis Raymond Jones, et al. Saturated reconstruction of a volume of neocortex. *Cell*, 162(3):648–661, 2015.

Kevin FH Lee, Cary Soares, Jean-Philippe Thivierge, and Jean-Claude Béïque. Correlated synaptic inputs drive dendritic calcium amplification and cooperative plasticity during clustered synapse development. *Neuron*, 89 (4):784–799, 2016.

Seok-Jin R Lee, Yasmin Escobedo-Lozoya, Erzsebet M Szatmari, and Ryohei Yasuda. Activation of camkii in single dendritic spines during long-term potentiation. *Nature*, 458(7236):299–304, 2009.

Mathieu Letellier, Florian Levet, Olivier Thoumine, and Yukiko Goda. Differential role of pre-and postsynaptic neurons in the activity-dependent control of synaptic strengths across dendrites. *PLoS biology*, 17(6):e2006223, 2019.

Gary S Lynch, Thomas Dunwiddie, and Valentin Gribkoff. Heterosynaptic depression: a postsynaptic correlate of long-term potentiation. *Nature*, 266(5604):737–739, 1977.

Luca Magri and Matthew P Juniper. Adjoint-based linear analysis in reduced-order thermo-acoustic models. *International Journal of Spray and Combustion Dynamics*, 6(3):225–246, 2014.

Guy Major, Alon Polsky, Winfried Denk, Jackie Schiller, and David W Tank. Spatiotemporally graded nmda spike/plateau potentials in basal dendrites of neocortical pyramidal neurons. *Journal of neurophysiology*, 99 (5):2584–2601, 2008.

Hiroshi Makino and Roberto Malinow. Compartmentalized versus global synaptic plasticity on dendrites controlled by experience. *Neuron*, 72(6):1001–1011, 2011. doi: https://doi.org/10.1016/j.neuron.2011.09.036.

Masanori Matsuzaki, Naoki Honkura, Graham CR Ellis-Davies, and Haruo Kasai. Structural basis of long-term potentiation in single dendritic spines. *Nature*, 429(6993):761–766, 2004.

Edward F Moore. The shortest path through a maze. In *Proc. Int. Symp. Switching Theory, 1959*, pages 285–292, 1959.

Rosel M Mulkey and Robert C Malenka. Mechanisms underlying induction of homosynaptic long-term depression in area ca1 of the hippocampus. *Neuron*, 9(5):967–975, 1992.

Hideji Murakoshi, Hong Wang, and Ryohei Yasuda. Local, persistent activation of rho gtpases during plasticity of single dendritic spines. *Nature*, 472(7341):100–104, 2011.

Thomas Nevian and Bert Sakmann. Spine ca2+ signaling in spike-timing-dependent plasticity. *Journal of Neuroscience*, 26(43):11001–11013, 2006.

Won Chan Oh, Laxmi Kumar Parajuli, and Karen Zito. Heterosynaptic structural plasticity on local dendritic segments of hippocampal ca1 neurons. *Cell reports*, 10(2):162–169, 2015.

Zahid Padamsey, Lindsay McGuinness, Scott J Bardo, Marcia Reinhart, Rudi Tong, Anne Hedegaard, Michael L Hart, and Nigel J Emptage. Activity-dependent exocytosis of lysosomes regulates the structural plasticity of dendritic spines. *Neuron*, 93(1):132–146, 2017.

Alon Polsky, Bartlett W Mel, and Jackie Schiller. Computational subunits in thin dendrites of pyramidal cells. *Nature neuroscience*, 7(6):621–627, 2004.

Roger L Redondo and Richard GM Morris. Making memories last: the synaptic tagging and capture hypothesis. *Nature Reviews Neuroscience*, 12(1):17–30, 2011.

Jacqueline Rose, Shan-Xue Jin, and Ann Marie Craig. Heterosynaptic molecular dynamics: locally induced propagating synaptic accumulation of cam kinase ii. *Neuron*, 61(3):351–358, 2009.

Sébastien Royer and Denis Paré. Conservation of total synaptic weight through balanced synaptic depression and potentiation. *Nature*, 422(6931):518–522, 2003.

Jonathan E Rubin, Richard C Gerkin, Guo-Qiang Bi, and Carson C Chow. Calcium time course as a signal for spike-timing–dependent plasticity. *Journal of neurophysiology*, 93(5):2600–2613, 2005.

Jackie Schiller, Guy Major, Helmut J Koester, and Yitzhak Schiller. Nmda spikes in basal dendrites of cortical pyramidal neurons. *Nature*, 404(6775):285–289, 2000.

Erin M Schuman and Daniel V Madison. Locally distributed synaptic potentiation in the hippocampus. *Science*, 263(5146):532–536, 1994.

Harel Z Shouval, Mark F Bear, and Leon N Cooper. A unified model of nmda receptor-dependent bidirectional synaptic plasticity. *Proceedings of the National Academy of Sciences*, 99(16):10831–10836, 2002.

Alcino J Silva, Richard Paylor, Jeanne M Wehner, and Susumu Tonegawa. Impaired spatial learning in α-calcium-calmodulin kinase ii mutant mice. *Science*, 257(5067):206–211, 1992.

Calum S Skene, Maximilian F Eggl, and Peter J Schmid. A parallel-in-time approach for accelerating direct-adjoint studies. *Journal of Computational Physics*, 429:110033, 2021.

Luc Stoppini, P-A Buchs, and Dominique Muller. A simple method for organotypic cultures of nervous tissue. *Journal of neuroscience methods*, 37(2):173–182, 1991.

Soon-Eng Tan and Keng-Chen Liang. Spatial learning alters hippocampal calcium/calmodulin-dependent protein kinase ii activity in rats. *Brain research*, 711(1-2):234–240, 1996.

Rudi Tong, Thomas Edward Chater, Nigel John Emptage, and Yukiko Goda. Heterosynaptic cross-talk of pre-and postsynaptic strengths along segments of dendrites. *Cell Reports*, 34(4):108693, 2021.

Jochen Triesch, Anh Duong Vo, and Anne-Sophie Hafner. Competition for synaptic building blocks shapes synaptic plasticity. *Elife*, 7:e37836, 2018.

Hidetoshi Urakubo, Miharu Sato, Shin Ishii, and Shinya Kuroda. In Vitro Reconstitution of a CaMKII Memory Switch by an NMDA Receptor-Derived Peptide. *Biophysical Journal*, 106(6):1414–1420, March 2014. ISSN 0006-3495. doi: 10.1016/j.bpj.2014.01.026. URL `https://doi.org/10.1016/j.bpj.2014.01.026`.

Shao-Nian Yang, Yun-Gui Tang, and Robert S Zucker. Selective induction of ltp and ltd by postsynaptic [ca2+] i elevation. *Journal of neurophysiology*, 81(2):781–787, 1999.

Ryohei Yasuda and Hideji Murakoshi. The mechanisms underlying the spatial spreading of signaling activity. *Current opinion in neurobiology*, 21(2):313–321, 2011.

Supplemental material

ROI detection algorithm

To identify a spine ROI, we needed to (*i*) identify the dendrite position and (*ii*) manually select the spine centre. To identify the dendrite position, we clicked on the beginning and end of the dendrite stretch of interest, and a breadth-first search (Moore, 1959) identified the dendritic path. We first needed to determine a putative spine centre to calculate the spine ROI by manually selecting the centre coordinate x_0. Once the spine centre was obtained, the ROI was calculated by stepping outward, pixel by pixel, on eight rays that formed an irregular octagon. Next, our algorithm checked if the following rules were met at each step, and if any of them were broken, a counter (also called a strike) was increased proportionally at each point where a strike occurred. A strike was added if the following conditions were met:

1. **Boundary Rule**
   If the ROI ray exceeds the boundary of the image, this ends the progression in that direction.
2. **Contour Rule**
   The image is treated with a Canny edge detection algorithm which calculates edges in an image. Depending on the distance from x_0, encountering such an edge counts as a certain number of strikes.
3. **Luminosity Fall-off Rule**
   Suppose the luminosity of the test point becomes one-third of the initial luminosity of x_0, or the luminosity falls below four times the background. In that case, the algorithm counts this rule as broken.
4. **Dendrite Rule**
   We assume that the spine is on average symmetrical and that the user will select the centre of the spine. Therefore, assuming that the initial point x_0 is outside the dendrite, this rule is broken once the test point is closer to the centre of the dendrite than to x_0.
5. **Luminosity Increase Rule**
   Suppose the luminosity increases on consecutive steps away from x_0. In that case, we have most probably entered the dendrite, and so after a certain amount of steps, we also consider this a rule break.

Once all rays have stopped, the ROI is drawn by connecting the eight points into an irregular octagon encompassing the spine. We used this octagon ROI to determine the luminosity quantities and calculate its area. To determine the interior of the ROI, we use a simple test involving the winding number algorithm (Hormann and Agathos, 2001), which sums up the angles subtended by each side of the polygon. If this number is non-zero, the test point is inside the polygon.

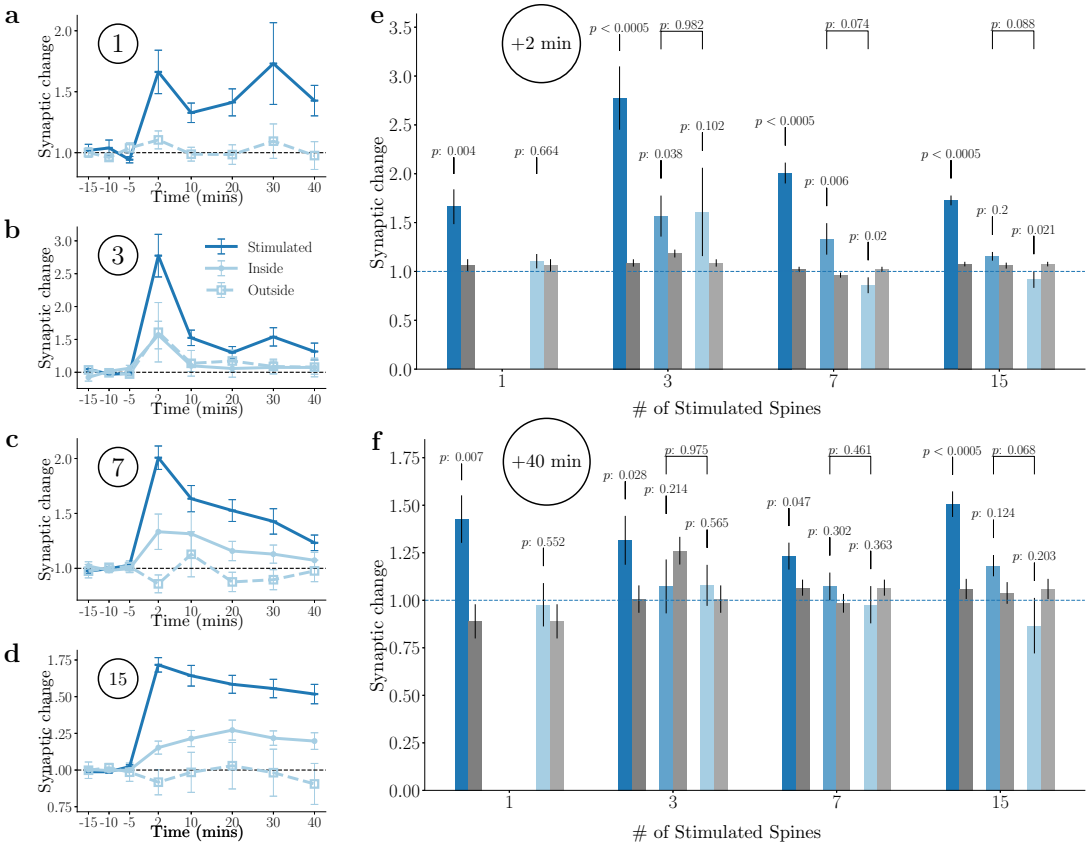

Figure S1: *After sLTP induction, stimulated spines and inside neighbour spines both grow while the outside neighbour spines (< 2μm) decrease* **a)-d)** Comparative plot of the stimulated, inside neighbour and outside neighbour spines for the single spine, three spine, seven spine and 15 spine paradigm, respectively. **e)** Normalised growth of control conditions of the stimulated, inside neighbour and outside neighbour spines at $t = 2$ minutes. The grey refers to the respective outside neighbours of the sham set. * signifies $p < 0.05$. **f)** Normalised growth of control conditions of the stimulated, inside neighbour and outside neighbour spines at $t = 40$ minutes. The grey refers to the respective outside neighbours of the sham data set.

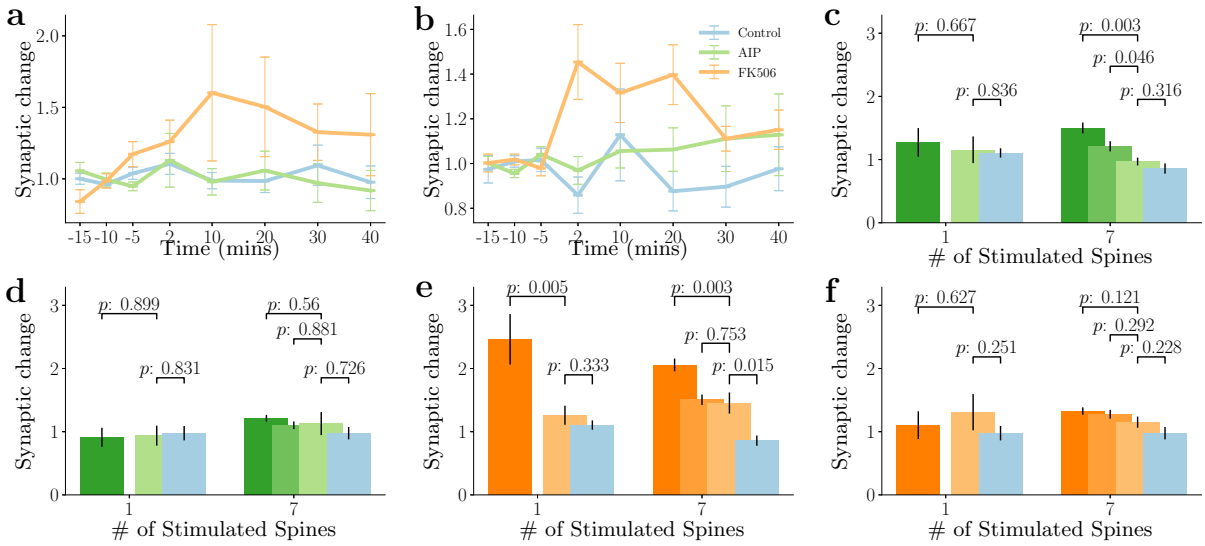

Figure S2: *The drug conditions have similar effects on the outside neighbour spines ($< 2\mu m$) as the stimulated set.* **a)** Comparative plot of the outside neighbour spines for the single spine condition. Shown are the Control, AIP and FK506 conditions. **b)** Comparative plot of the outside neighbour spines for the seven spine condition. Shown are the Control, AIP and FK506 conditions. **c)-d)** Normalised growth of the AIP condition for the stimulated and outside neighbour spines at $t = 2$ minutes and $t = 40$ minutes, respectively. The blue refers to the respective outside neighbours of the control set. * signifies $p < 0.05$. **e)-f)** Normalised growth of the FK506 condition for the stimulated and outside neighbour spines at $t = 2$ minutes and $t = 40$ minutes, respectively. The blue refers to the respective outside neighbours of the control set.

Details on the parameter fitting algorithm

Here, we present the equations that drive the gradient-based adjoint approach(Magri and Juniper, 2014) described in the model analysis section but will omit the derivation thereof as it lies outside the scope of this article. Direct solutions of the gradients are evaluated numerically to acquire the required parameter updates. The first three equations define the adjoint state variables (denoted by the $(\cdot)^\dagger$) that deliver the sensitivity information of the model to changes in the parameters. The parameters without the dagger remain the same as those observed in the governing model equations. Finally, $\hat{L}_{x,t}$ was introduced in the numerical methods section and denotes the averaged spine

$$\frac{\partial C^\dagger}{\partial t} = \alpha C^\dagger - \beta_1 P^\dagger - \zeta_1 S^\dagger \tag{7}$$

$$\frac{\partial P^\dagger}{\partial t} = -\zeta_2 S^\dagger \frac{\partial F(P)^\dagger}{\partial P} + \beta_2 P^\dagger \tag{8}$$

$$\frac{\partial S^\dagger}{\partial t} = 2 \sum_{x=0}^{X} \sum_{t=0}^{T} (S(x,t) - \hat{L}_{x,t}) \tag{9}$$

The following equations denote the required calculations involving both the model and adjoint variables to calculate the gradient that will lead to better fits. Each of these gradients is denoted by the variable we wish

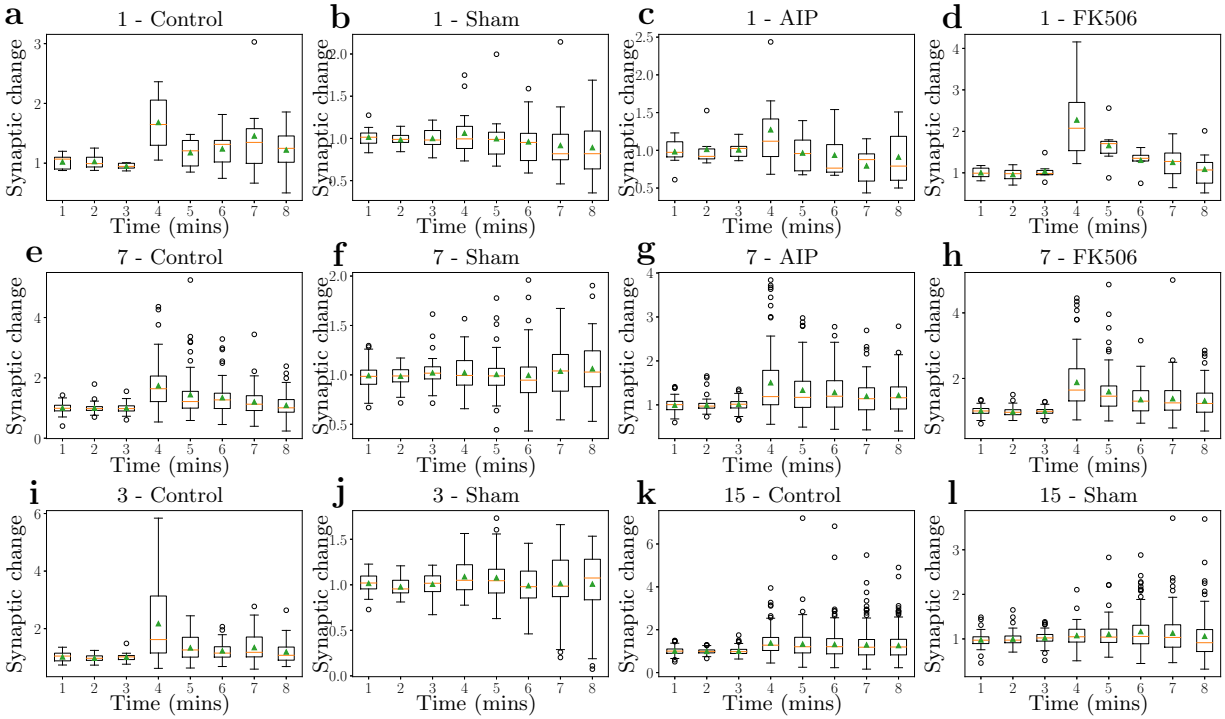

Figure S3: **a) - d)** Experimentally recorded statistics of the stimulated spines in experiments with 1, 3, 7 or 15 stimulated spines. Lower to upper quartile values of the data are shown, with a line denoting the median. The whiskers refer to 1.5 times the IQR. Data points outside the whiskers are considered outliers. The green triangle refers to the mean of the data. **e) - f)** Dynamics of the seven spine experiment with the four different paradigms. **i) - j)** Dynamics of the three spine experiment for the control and sham. **k) - l)** Dynamics of the 15 spine experiment for the control and sham.

to change and the superscript †.

$$C_0^\dagger = C^\dagger|_{t=0} \tag{10}$$

$$P_0^\dagger = P^\dagger|_{t=0} \tag{11}$$

$$\alpha^\dagger = -\sum_{t=0}^{T} C^\dagger C \tag{12}$$

$$\beta_1^\dagger = -\sum_{t=0}^{T} P^\dagger C \tag{13}$$

$$\beta_2^\dagger = \sum_{t=0}^{T} P^\dagger P \tag{14}$$

$$\zeta_1^\dagger = \sum_{t=0}^{T} S^\dagger C \tag{15}$$

$$\zeta_2^\dagger = \sum_{t=0}^{T} S^\dagger F(P) \tag{16}$$

$$\nu_1^\dagger = -\zeta_2 \sum_{t=0}^{T} S^\dagger \frac{\partial F(P)^\dagger}{\partial \nu_1} \tag{17}$$

$$\nu_2^\dagger = -\zeta_2 \sum_{t=0}^{T} S^\dagger \frac{\partial F(P)^\dagger}{\partial \nu_2} \tag{18}$$

Given these equations a simple example update step would then be

$$\alpha_{\text{new}} = \alpha_{\text{old}} + \alpha^\dagger \tag{19}$$

We thus iterate over our parameters until no more change is observed in the update values.

Parameter optimisation per experiment

Here we report the number of experiments and selected spines for each experimental condition. All of these points were acquired through the semi-automatic python tool with manual re-correction in $\approx 5\%(81)$ of the spines.

Experiment	Reference figures	Reference data set	C_0	P_0	α	$\beta_{1,2}$	$\zeta_{1,2}$	$\nu_{1,2}$
Three spine	Fig. 3b, c & f, Fig. 6	N/A	✓	✓	✓	✓	✓	✓
Three spine (I.N.)	Fig. 3b, c & f, Fig. 6	Three spine	✓	✓				✓
Single spine	Fig. 2b, c, d, g & h, Fig. 6	Three spine	✓	✓				✓
Single spine (AIP)	Fig. 2c, d, g & h	Single spine		✓				✓
Single spine (FK506)	Fig. 2c, d, g & h	Single spine		✓				✓
7 spine	Fig. 4b, c, d, f & g, Fig. 6	Three spine	✓	✓				✓
7 spine (AIP)	Fig. 4c, d, f & g	7 spine		✓				✓
7 spine (FK506)	Fig. 4c, d, f & g	7 spine		✓				✓
7 spine (I.N.)	Fig. 4b, c, e & g, Fig. 6	7 spine	✓	✓				✓
7 spine (AIP, I.N.)	Fig. 4e & g	7 spine (I.N.)		✓				✓
7 spine (FK506, I.N.)	Fig. 4e & g	7 spine (I.N.)		✓				✓
15 spine	Fig. 5b, c & f, Fig. 6	Three spine	✓	✓				✓
15 spine (I.N.)	Fig. 5b, c & f, Fig. 6	15 spine	✓	✓				✓

Table 1: Model parameters that were fit per experimental paradigm. If an entry has a ✓ then this indicates that this parameter has been altered with respect to the corresponding reference parameter set and which is noted in the "Reference set" column. A lack of a checkmark means that the parameters were carried over from the fit of the reference data set. Other fitting pathways (i.e., using the I.N.s of the three spine experiment to fit the I.N. of the seven spine paradigm) were also explored, but no discernable difference was discovered.

Experiment	Reference figures	# of Expts	Stimulated spines	# of I.N.	# of O.N.
Single spine	Fig. 2 & Fig. 6	7	7		7
Single spine (sham)	Fig. 2 & Fig. 6	18	18		30
Single spine (AIP)	Fig. 2 & Fig. 6	9	9		16
Single spine (FK506)	Fig. 2 & Fig. 6	7	7		11
Three spine	Fig. 3 & Fig. 6	8	23	14	20
Three spine (sham)	Fig. 3 & Fig. 6	13	29	19	11
7 spine	Fig. 4 & Fig. 6	10	65	29	12
7 spine (sham)	Fig. 4 & Fig. 6	9	49	35	15
7 spine (AIP)	Fig. 4 & Fig. 6	12	81	54	28
7 spine (FK506)	Fig. 4 & Fig. 6	12	82	46	24
7 spine (Distributed)	Fig. 4 & Fig. 6	9	59	200	10
15 spine	Fig. 5 & Fig. 6	15	194	100	14
15 spine (sham)	Fig. 5 & Fig. 6	7	99	52	9

Table 2: Number of studied spine types per experiment. I.N. refers to the number of inside neighbour spines not present in the single spine paradigm, and O.N. refers to the outside neighbour spines.